UNIVERSITY OF CALIFORNIA
Santa Barbara

Growth of high-quality N-polar (000-1) GaN on bulk GaN by plasma-assisted molecular beam epitaxy for high electron mobility transistors

A thesis submitted in partial satisfaction of the
requirements for the degree
Master of Science
in
Electrical and Computer Engineering

By

Christian D. Wurm

Committee in charge:
Professor Umesh K. Mishra, Chair
Professor Steven P. DenBaars
Professor James S. Speck
Dr. Stacia Keller

September 2019

This thesis of Christian D. Wurm is approved.

Stacia Keller

James S. Speck

Steven P. Denbaars

Umesh K. Mishra, chair

June 2019

Growth of high-quality N-polar (000-1) GaN on bulk GaN by plasma-assisted molecular beam epitaxy for high electron mobility transistors

By

Christian D. Wurm

Acknowledgments

I would like to thank my loving Wife, Aidee Sarabia Wurm, who's love and support got me to where I am today. I could not have done any of this without her. I am extremely thankful for my parents, Mike and Sandy Wurm, my sister, Melissa Herskowitz, and my two nieces, Makenzie and Madeline Herskowitz for their continued love and support through all my years.

I am very grateful for my advisor prof. Umesh K. Mishra for letting me join his amazing group and for all that I have learned from him. The people of the Mishra group, in particular, have proven to be invaluable sources of information for all things related to gallium nitride (GaN) growth and technology. I would like to thank prof. Elaheh Ahmadi for having the time and patience to teach me most of what I know about plasma-assisted molecular beam epitaxy; Dr. Stacia Keller for being an invaluable source of information on all things related to epitaxial growth of GaN; Dr. Brian Romanczyk for being a walking encyclopedia on all things related to device processing and technology; and all the other people in the Mishra group including and not limited to Dr. Nirupam Hatui, Wenjian Liu, Dr. Xun Zheng, Dr. Cory Lund, Dr. Anchal Agarwal, Dr. Mathew Guidry, Dr. Onur Koksaldi, Dr. Steven Wienecke, Dr. Chirag Gupta, Shubhra Shweta, Athith Krishna, Pawana Shrestha, Weiyi Li and Aditya Raj.

I would also like to thank those I have worked with in the MBE lab at UCSB including Kelsey Jorgensen, Richard Cramer, John English, Erin Young, Christian Robertson, Jianfeng Wang, Kurt Olson and Clayton Qwah.

I am also indebted to my former colleagues and professors as UC San Diego who taught me so much and who played a major role helping get into UCSB. I am extremely

greatful for Prof. Shaya Fainmann for funding me in my early days working in the cleanroom; prof. Yuan Taur and prof. Shadi Dayeh, for always taking the time to talk to me outside of class and for teaching me so much. I am especially grateful for prof. S. S. Lau for all that he taught me and for pushing me to better understand semiconductor physics. I am also grateful for prof. Charles Tu for encouraging me to apply to schools that I never thought I had a chance to get into. I am also grateful for my fellow colleagues at UC San Diego including Dr. Hung-His Lin, Dr. Felipe Vallini, Dr. Rajat Sharma, Dr. Abdelkrim Al Amili, Dr. Shiva Shahin, Jordan Davis, Suruj Deka, Atsunori Tanaka and Dr. Namseok Park.

I am also personally indebted to Alan Street for introducing me to the world of semiconductor devices. Finally, I would like to thank all of the members of my committee for reviewing my thesis.

Christian D. Wurm

Curriculum Vitae

Education

- **University of California Santa Barbara** (2019-present)
  Pursuing PhD Degree in Electrical and Computer Engineering with an emphasis on electronics and photonics

- **University of California Santa Barbara** (2017-2019)
  Masters Degree in Electrical and Computer Engineering with an emphasis on electronics and photonics

- **University of California San Diego** (2014-2017)
  Bachelors Degree in Electrical and Computer Engineering with an emphasis on devices and materials

Work experience

- **University of California Santa Barbara** (2017-2019)
  Advisor: Umesh K. Mishra
  Graduate student researcher

- **Ultrafast and Nanoscale Optics group at UC San Diego** (2014-2017)
  Advisor: Prof. Shaya Fainman
  Student researcher

- **San Diego Mesa Community College** (2012-2014)
  Math, physics, chemistry and Chinese tutor

- **FieldLogix** (2008-2012)
  Field Service Specialist, operations representative, technical Support Representative

- **Syndicate Automotive Concepts** (2005-2007)
  Installer/Fabricator: Car audio, security, navigation and video installation, custom interior fabrication

- **Al and Ed's Autosound** (2004-2005)
  Installer, Install Bay Manager

Journal publications

- S. S. Pasayat, E. Ahmadi, B. Romanczyk, O. Koksaldi, A. Agarwal, M. Guidry, C. Gupta, C. Wurm, S. Keller and U.K. Mishra. “First demonstration of RF N-polar GaN HEMTs grown on Bulk GaN using PAMBE” Semiconductor Science and Technology, 2019

- C. Lund, M. Catalano, L. Wang, C. Wurm, T. Mates, M. Kim, S. Nakamura, S. DenBaars, U. Mishra, S. Keller. “Metal-organic chemical vapor deposition of N-polar InN quantum dots and thin films on vicinal GaN” Applied Physics Letters, 2018

- H.H. Lin, F. Vallini, M.H. Yang, R. Sharma, M. Puckett, S. Montoya, C. Wurm, E. Fullerton & Y. Fainman. “Electronic Metamaterials with Tunable Second-order Optical Nonlinearities” Scientific Reports, August 2017

- H.H. Lin, M.H. Yang, R. Sharma, M.Puckett, S. Montoya, C. Wurm, F. Vallini, E. Fullerton, Y. Fainman. “Synthesis of Second-order Nonlinearities in Dielectric-Semiconductor-Dielectric Metamaterials” Applied Physics Letters, Dec. 2016

Conference papers

- S. S. Pasayat, E. Ahmadi, B. Romanczyk, O. Koksaldi, A. Agarwal, M. Guidry, C. Gupta, C. Wurm, S. Keller and U.K. Mishra. “First demonstration of RF N-polar GaN HEMTs grown on Bulk GaN using PAMBE” Electronics Letters, 2018

- H.H. Lin, M.H. Yang, R. Sharma, M.Puckett, S. Montoya, C. Wurm, F. Vallini, E. Fullerton, Y. Fainman. “Engineering of Second-Order Nonlinearity in Silicon-dielectric Multilayers” CLEO Conference, June 2016

- H.H. Lin, R. Sharma, M.H. Yang, M. Puckett, C. Wurm, F. Vallini, and Y. Fainman “Enhanced Effective Second-order Nonlinearities in Si-rich SiNx Thin Films” CLEO Conference, May 2017

Abstract

Growth of high-quality N-polar (000-1) GaN on bulk GaN by plasma-assisted molecular beam epitaxy for high electron mobility transistors

by

Christian D. Wurm

Recently reported N-polar gallium nitride (GaN) high electron mobility transistors (HEMTs) have shown exceptional W-band (75-110 GHz) performance, surpassing current Ga-polar device technology in terms of output power performance. This is in part due to the incredible progress made in the growth and optimization of N-polar GaN in the last decade, despite the many problems associated with the unstable N-polar surface. Top performing GaN devices, reported today, are all grown by MOCVD on foreign substrates such as SiC. Growing on foreign substrates where lattice mismatch is present leads to a high density of threading dislocations (TDs) which generate at the substrate/epi interface and propagate in the growth direction, terminating on the surface. These TDs can act as coulombic scattering centers, and, in the case of MBE, lead to vertical leakage and roughen the GaN surface. Although growing thick MOCVD buffer layers has shown to decrease the density of these TDs by almost two orders of magnitude, the resulting TD-density is still typically two orders of magnitude higher than what is found in high-quality bulk-GaN substrates.

Amplifiers biased in class-A mode operate with at a high source-to-drain quiescent current. High channel current in a material with a high density of scattering centers may lead to power dissipation in the form of heat which can impede device efficiency – something which could be improved by growing devices on bulk GaN substrates with an order of magnitude or lower TDD. In addition to dislocation scattering, alloy scattering has shown to

be a significant inhibitor of mobility in GaN HEMTs. Using MBE, which typically utilized growth temperatures much lower than MOCVD, thicker coherently strained AlN interlayers or back-barriers can be realized to mitigate the effects of alloy scattering.

Although it has been shown in the past that GaN grown on bulk GaN by MBE resulted in a surface with a high density of pits and depressions, the work presented here demonstrates how smooth high-quality GaN can be grown on non-miscut bulk-GaN substrates. Although the pits seen on the surface of GaN grown on bulk GaN may come from a variety of factors, evidence presented in this work reveals that surface impurities play a significant role in the generation of these pit. By employing an ex-sity UV-ozone surface clean and initiating growth with a thin layer of AlN grown under Ga-rich conditions, high-quality, pit-free, N-polar GaN surfaces were obtained by MBE.

Several device structures using pure AlN back-barriers with thicknesses ranging from 2-6 nm were simulated and it was found that using a 30 nm graded AlGaN layer behind a 2 nm or 6 nm AlN back-barrier resulted in a 2DEG sheet charge density around $4x10^{13}$ cm^{-2}, approximately 3-4x larger than what has been reported in current N-polar HEMT structures. Whether or not these devices can be realized will depend on how much strain the AlN backbarrier and graded AlGaN region can sustain without relaxation – something with is subject to further study. From this work, however, we now have the tools to grow more complex N-polar HEMT structures on bulk GaN by MBE which may one day surpass current N-polar HEMT technology.

Table of contents

Figures

Tables

Chapter 1: Introduction

This thesis focuses on the motivation for developing N-polar gallium nitride (GaN) high electron mobility transistors (HEMTs) grown by molecular beam epitaxy (MBE) on bulk GaN substrates for applications in high-power high-frequency electronics.

1.1 Introduction:

The motivation behind N-polar homoepitaxially MBE-grown HEMTs comes from its application in high-frequency and high-power electronics. Factors such as polarization-doping, high-bandgap, high mobility and high saturation velocity have enabled GaN-based microwave amplifier technology to penetrate both the defense and civilian market in recent years. Although GaN has a lower intrinsic bulk mobility with respect to GaAs (~1000 cm^2/Vs compared to ~8500 cm^2/Vs respectively), its higher bandgap (3.4eV compared to 1.42eV in GaAs) and high electron saturation velocity (2e7 cm/s) [6] enables device engineers to build HEMTs which operate at higher frequency and higher power compared with GaAs HEMTs [1]. Although GaN-based technology currently deployed in the market consist mainly of Ga-polar devices, N-polar GaN HEMT technology has made considerable progress in the past decade surpassing current Ga-polar HEMT technology in terms of W-band power performance [2], [3].

The majority of N-polar GaN HEMT technology showing the highest performance metrics are all based on devices grown by MOCVD on foreign substrates. To understand the potential advantage homoepitaxy has over heteroepitaxy one must understand dislocations and how they can negatively affect device performance. Understanding why MBE grown devices may be advantageous over MOCVD grown devices lies in

understanding the versatility of MBE. A key part of this thesis is to help the reader to understand that while MOCVD-grown devices on foreign substrates show exceptional results there still exists an interest in pursuing MBE-grown devices on bulk-GaN. Before this can be done, however, one must understand the basics of III-nitride based HEMTs.

1.2 Gallium nitride and polarization doping

What sets GaN apart from traditional semiconductors, besides its high-bandgap and mobility, is its crystal structure. Although GaN and most III-nitrides have been grown in the zinc-blend phase the wurtzite phase is the more stable of the two. Wurtzite GaN is a non-centrosymmetric crystal structure. Because of this, alternating polarization sheet charges exist along the c-axis (000+/-1 direction). Although each of these internal polarization-induced sheet charges are effectively screened by the oppositely charged sheet-charge preceding it, there will exist an internal net electric field in the crystal due to the opposing polarization sheet charges at the opposing crystal faces. Figure 1.2.1 below shows the crystal structure of GaN and how polarization charges at each end of the crystal lead to a built-in electric field. The N-polar orientation is simply the Ga-polar orientation flipped upside down; electric field and band bending are reversed along the c-plane when flipped. The spontaneous polarization field in GaN is approximately -0.029 C/m^2 [6] or a corresponding spontaneous polarization charge density $n_\pi \sim 10^{13} cm^{-2}$ [4]. As the GaN grows in the c-direction this internal electric field must be maintained due to the opposing polarization sheet charges, therefor the conduction band and valence band continue to bend as a function of depth until the Fermi-level intersects with some donor-trap state in the bandgap. As this donor trap

ionizes and the film continues to grow, the spontaneous polarization charge at each end gets effectively screened by the charged donor state and the internal electric fields cancel [4].

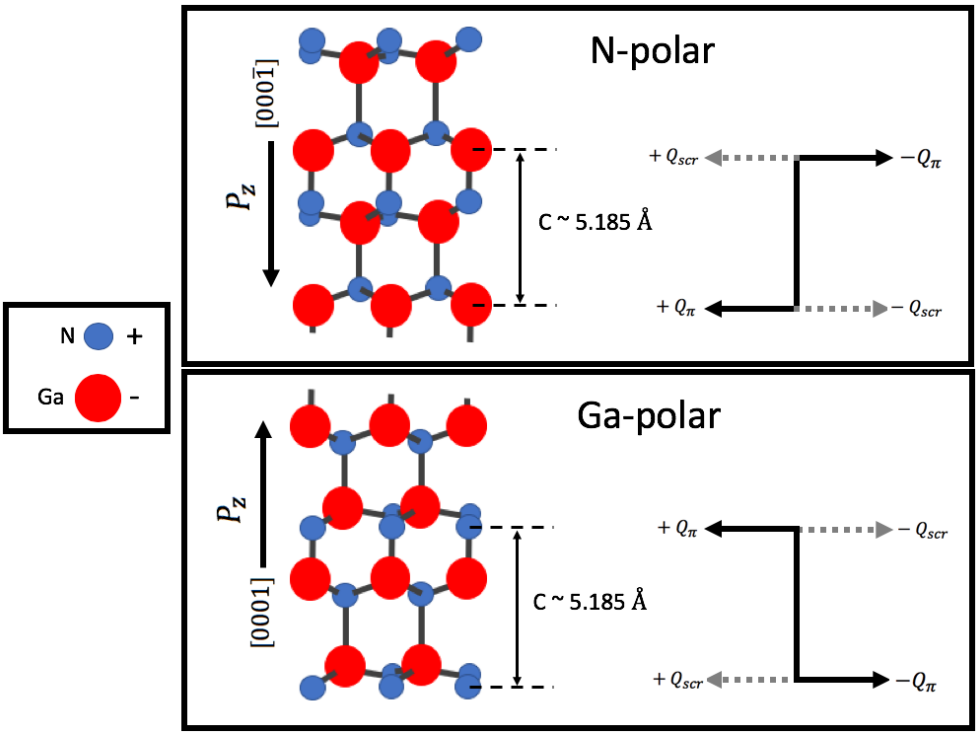

Figure 1.2.1: Wurtzite GaN unit cell showing polarization charges for N-polar (top) and Ga-polar (bottom)

Just as important as the spontaneous polarization inherent in III-nitride films is the piezoelectric polarization which occurs in strained heterostructures. The piezoelectric tensor of wurtzite has three non-vanishing independent components making wurtzite GaN highly piezoelectric [5]. This means that wurtzite GaN will produce additional polarization charge, in addition to the spontaneous polarization already present, when subjected to in-plane strain. Anytime there is a heterostructure, such as AlGaN/GaN, with an in-plane lattice mismatch, strain occurs. In III-nitrides, assuming a heterostructure that is fully strained to GaN, this strain leads to a piezoelectric sheet charge at the heterointerface which is dependent on the

strain-moduli components (e_{33} and e_{31}), the elastic coefficients (c_{13} and c_{33}) and the lattice constant of both materials given by:

$$P_{pz,[0001]} = 2(e_{31} - e_{33}\frac{c_{13}}{c_{33}})\epsilon_1 \tag{1.1}$$

Where the in-plane strain ϵ_1 arising from the lattice mismatch of the heterostructure is given by:

$$\epsilon_1 = \frac{a_i - a_{GaN}}{a_{GaN}} \tag{1.2}$$

Where a_i is the lattice constant of the material strained to GaN and can be found by Vegard's law [7]. The total polarization field at a hetero-interface is the sum of the spontaneous polarization and the lattice mismatch dependent piezoelectric polarization field. Hence the net polarization induced sheet charge at a hetero-interface is a strong function of lattice mismatch between GaN and the material strained to GaN. Fig. 1.2.2 below shows the polarization sheet charge for an GaN/AlGaN hetero-interface as a function of Al-mole fraction.

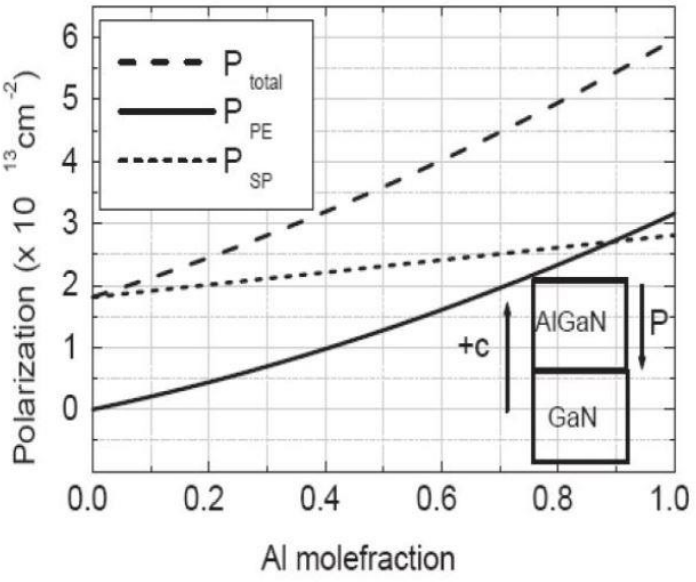

Figure 1.2.2: polarization vs. Al mole fraction graph [8]

The resulting charge profile, electric field and energy band diagram for a Ga-polar and N-polar (GaN/AlGaN & GaN/AlGaN/GaN respectively) is shown in Fig. 1.2.3 below.

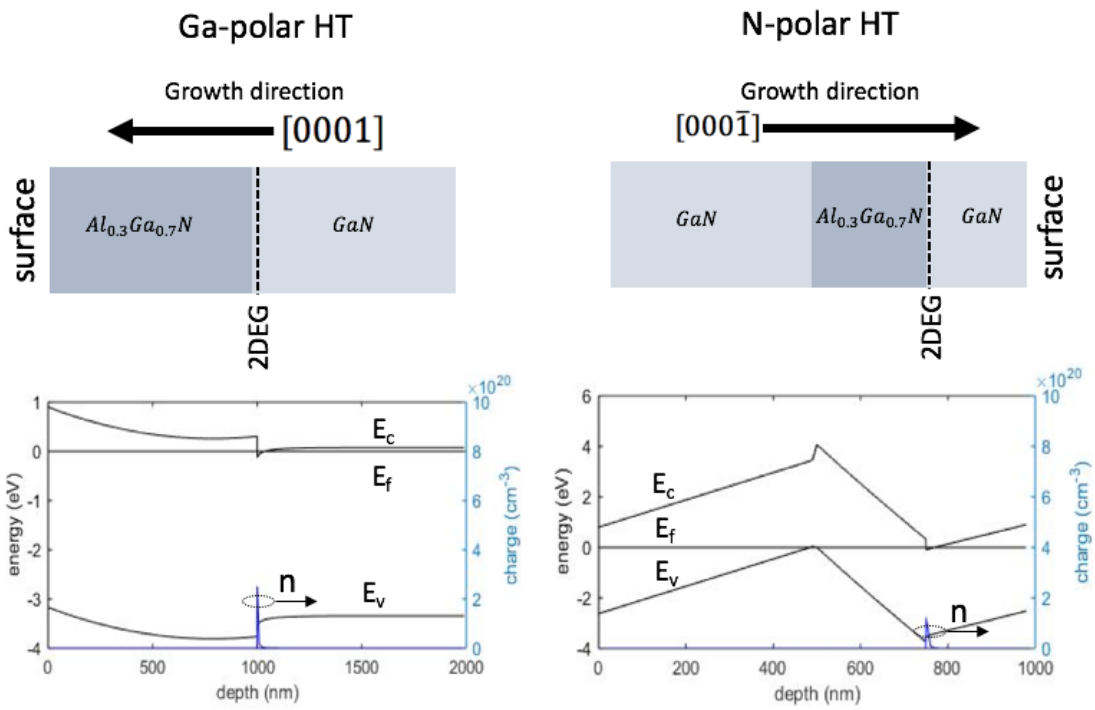

Figure 1.2.3: Ga polar (left) and N-polar (right) energy band diagrams for AlGaN/GaN hetero-structures (HT) as a function of depth

The large positive polarization-induced sheet charge at the heterointerface in 1.2.3 leads to an electron sheet charge in the GaN close to the heterointerface which serves as the channel for GaN/AlGaN HEMTs. This electron sheet charge is referred to as the 2-dimentional electron-gas or 2DEG. Unlike GaAs and InP based HEMTs in which the 2DEG channel comes from an impurity-doped sheet charge in the high-bandgap barrier, the 2DEG in GaN HEMTs comes from the periodic polarization charges along the hetero-interface. This means that when a current is induced due to a lateral electric field (adjacent to growth direction) there will be no scattering of the 2DEG channel due to remote-ionized impurities

such as in the case of a GaAs/AlGaAs heterostructure. The result of this polarization-doped heterostructure is a channel mobility that can surpass the bulk mobility of the material.

1.3 Ga-polar vs. N-polar heterostructures:

It is important to note the distinction in the two crystal orientations shown in Fig. 1.2.1 and in figure 1.2.3. Looking back at Fig. 1.2.2, the N-polar orientation, also known as the N-face or (000-1) orientation, has the spontaneous polarization vector pointing downward – opposite to that of the Ga-polar polarization vector. Thus, one can invert the crystal polarity by simply flipping the crystal 180º. This is not to be confused with the terms 'Ga-terminated' or 'N-terminated' which refers to the atoms on the surface of the crystal; one does not invert the polarity of the GaN crystal by simply removing the top atomic-layer because the polarity is inherent to the crystal structure [5].

The band diagram of the N-polar and Ga-polar heterostructures alone do not give a full picture of the advantages N-polar HEMTs have over Ga-polar HEMTs. Understanding the advantages of N-polar HEMTs lies in the device architecture. Fig. 1.2.4 below shows a basic planer N-polar HEMT structure. Firstly, we see that the AlGaN layer acts as a natural backbarrier which confines the 2DEG to the GaN layer between the surface and the AlGaN backbarrier (known as the channel region) thereby reducing buffer leakage and increasing channel to bulk capacitance. This natural backbarrier also helps with scalability reducing the effects of drain-induced barrier lowering (DIBL) as the channel length is scaled. This natural backbarrier effect can be compared to that of silicon-on-insulator (SOI) technology used in many modern CMOS foundries. Another advantage of N-polar HEMTs is that source and drain contacts can be made by etching into the channel and regrowing n+ GaN - making

direct contact with the 2DEG without having to etch through the AlGaN barrier. These regrown n+ contacts provide ultralow contact resistance for the source and drain, greatly improving device performance.

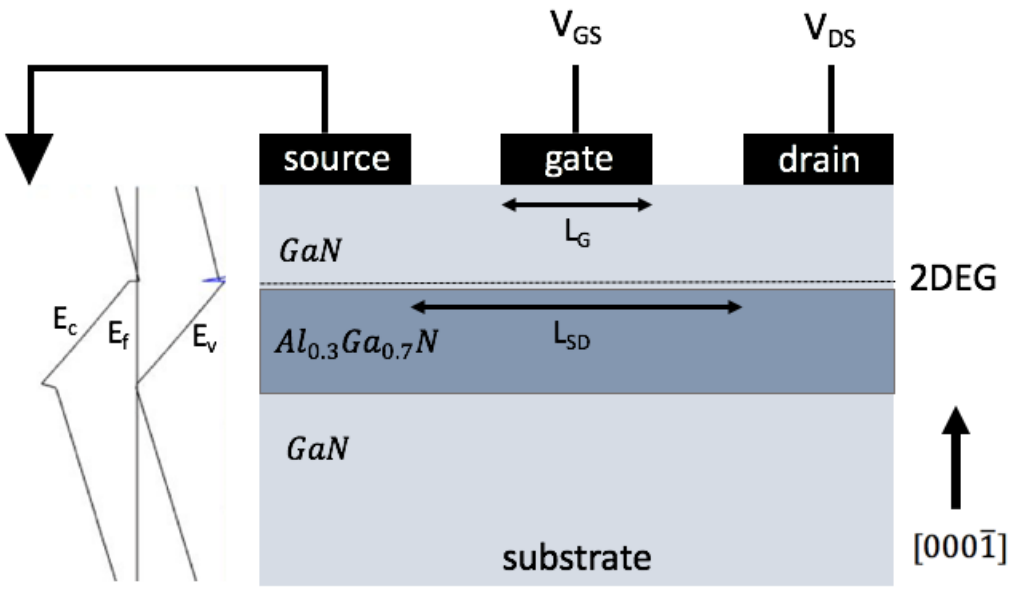

Figure 1.2.4: Simplified planar N-polar HEMT structure. Corresponding band-diagram to the left of the diagram. Note: L_G is the gate length and L_{SD} is the distance between the source and drain. The region of the channel directly under the gate is controlled by V_{GS}.

1.4 Overview of thesis:

In the chapter to follow a general history of N-polar GaN HEMT technology will be given. This chapter will focus primarily on heteroepitaxially grown devices by both MBE and MOCVD. Chapter three, which is primarily focuses on the motivation behind MBE-grown homoepitaxially grown HEMTs, will begin with a general description of plasma-assisted molecular beam epitaxy (PAMBE) and Ga-rich growth of III-nitride films by PAMBE followed by an overview of how dislocations can impede device performance and the advantages MBE has over MOCVD. Chapter four will describe, in-depth, the studies

which were carried out to achieve high quality N-polar GaN films grown on bulk GaN substrates. Chapter five will present some proposed N-polar HEMT structures which could be grown on bulk GaN substrates by PAMBE.

References:

[1] U. K. Mishra, P. Parikh, and Y.-F. Wu, "AlGaN/GaN HEMTs-an overview of device operation and applications," *Proc. IEEE*, vol. 90, no. 6, pp. 1022–1031, Jun. 2002.

[2] B. Romanczyk *et al.*, "Demonstration of Constant 8 W/mm Power Density at 10, 30, and 94 GHz in State-of-the-Art Millimeter-Wave N-Polar GaN MISHEMTs," *IEEE Trans. Electron Devices*, vol. 65, no. 1, pp. 45–50, Jan. 2018.

[3] S. Wienecke *et al.*, "N-Polar GaN Cap MISHEMT With Record Power Density Exceeding 6.5 W/mm at 94 GHz," *IEEE Electron Device Lett.*, vol. 38, no. 3, pp. 359–362, Mar. 2017.

[4] U. K. Mishra and J. Singh, *Semiconductor device physics and design*. Dordrecht: Springer, 2008.

[5] O. Ambacher, "Growth and applications of Group III-nitrides," *J. Phys. Appl. Phys.*, vol. 31, no. 20, pp. 2653–2710, Oct. 1998.

[6] E. archive New Semiconductor Materials Characteristics and Properties

[7] *http://www.ioffe.rssi.ru/SVA/NSM/*.

[8] D. Jena, Thesis (2002)

[9] unknown source

Chapter 2: N-polar GaN HEMT technology

2.1 Introduction:

In order to understand the motivation for studying homoepitaxially grown N-polar HEMTs by MBE it is necessary to understand the evolution of N-polar HEMT technology. N-polar GaN devices have made more progress in the last decade than ever before. The devices discussed in this chapter were all heteroepitaxially grown structures; that is, devices grown on foreign substrates. When discussing heteroepitaxy vs. homoepitaxy in this dissertation we are referring to structures grown on foreign vs. native substrates respectively – an important distinction to point out as almost all III-nitride HEMT structures rely on channels produced from heterointerfaces grown far from the substrate/growth interface.

In the first part of this chapter we summarize a few of the figures of merit (FOM) which are used in characterizing HEMTs followed by a history of N-polar GaN HEMT technology. The evolution of N-polar III-nitride growth by both MOCVD and MBE and the record-breaking FOMs of the most recently published N-polar HEMTs will be discussed. The motivation behind homoepitaxially grown HEMT structures will segue into the following chapter which will go into the motivation for MBE homoepitaxially grown devices.

2.2 HEMT figures of merit (FOMs):

There are many figures of merit used to characterize HEMTs. Without going into specific detail of the characterization techniques used to obtain these FOMs we can at least summarize some important FOMs used to define HEMT performance. The common starting point for characterizing HEMT epi (epitaxial grown HEMT structure) is by Van Der Paw

Hall which gives a sheet charge carrier density (n_s), carrier mobility (μ) and sheet resistance (R_s) measured in $\Omega/\blacksquare$. Transfer length measurements are also used to extract R_s as well as contact resistance, such as that of the metal/semiconductor interface. Load-pull measurements are used to extract large signal device parameter such as output power P_o (given in watts/mm) and power added efficiency (PAE) for a given frequency and source-drain bias V_{DS} where:

$$PAE \triangleq \frac{P_{out}-P_{in}}{P_{DC}} = DE(1-\frac{1}{G_p}) \tag{2.1}$$

Where DE, G_p and G_T are the drain efficiency, operating power gain and transducer gain respectively given by:

$$DE \triangleq \frac{P_{out}}{P_{DC}} \tag{2.2}$$

$$G_p \triangleq \frac{P_{out}}{P_{in}} \tag{2.3}$$

$$G_T \triangleq \frac{P_{out}}{P_{in,ave}} \tag{2.4}$$

f_T and f_{max} are the high power-gain cutoff frequency and maximum current gain frequency respectively and are commonly measured using a network analyzer. Transconductance is a measure of the rate of change of gate voltage (V_g) and drain current (I_d); it is a parameter that describes how the gate modulates the channel and has a profound effect on the linearity of the device. Transconductance is given by:

$$g_m = \frac{dI_D}{dV_g} \tag{2.5}$$

There are countless more FOMs used in characterizing HEMTs. An in-depth description of these FOMs and how they are attained is well outside the scope of this thesis. A more through explanation of large signal and small signal device parameters can be found in [1].

2.3 Evolution of GaN HEMT technology (2007-2018):

In addition to scalability and low source and drain contact resistance, N-polar GaN HEMTs have many more advantages over their Ga-polar counterparts such as the ability to use deep-recessed T-gates, nearly-pure AlN interlayers and GaN caps. However, to better understand how these other device characteristics make N-polar HEMTs a superior technology in high-power mm-wave electronics one must understand how the technology has evolved into what it is today. Table 2.3.1 below gives the large-signal metrics for a variety of N-polar HEMTs published between 2007-2018; table 2.3.2 below shows the small-signal metrics from devices which were published between 2007-2018. Fig. 2.3.6 below shows a general evolution of N-polar device architecture described in this section. As will be shown below, the early N-polar HEMTs developed by MBE were inferior compared with the Ga-polar technology of that time. Later, the development of MOCVD grown N-polar GaN pushed device metrics to a new level. Eventually, with the development of deep-recessed gate technology, W-band devices which could compete with Ga-polar devices of that time were realized. The following sub-section will go more in-depth on each of these devices and how the device architecture evolved into what it is today.

Table 2.3.1: Large-signal device metrics for N-polar devices published from 2007-2018. Note: L_g is the gate length, 'fg' stands for foot-gate (bottom part of deep-recess gate – see Fig. 2.3.5).

Ref	growth method	sub.	Lg (nm)	V_{ds} (volts)	P_o (W/mm)	PAE (%)	G_T (dB)
[2]	MBE	SiC	700	40	4.5	34	10.3
[3]	MBE	SiC	700	35	7.1	58	15.3
[4]	MBE	SiC	700	40	8.1	54	12.7
[4]	MBE	SiC	700	35	6.7	56	-
[4]	MBE	SiC	600	20	4.1	71	13.1
[4]	MBE	SiC	600	28	6.4	67	13.1
[5]	MBE	SiC	700	28	5.7	56	7.1
[6]	MOCVD	Al2O3	700	50	12.1	55	9.8
[6]	MOCVD	Al2O3	700	30	5.9	64	-
[7]	MOCVD	SiC	700	30	5.7	74.5	-
[7]	MOCVD	SiC	700	58	16.7	44	-
[7]	MOCVD	SiC	700	70	20.7	60	-
[8]	MOCVD	Al2O3	60 (fg)	8	1.6	16.5	-
[8]	MOCVD	Al2O3	60 (fg)	14	4.2	-	4.2
[9]	MOCVD	Al2O3	70 (fg)	8	1.73	20	-
[9]	MOCVD	Al2O3	70 (fg)	10	2.9	15.5	-
[10]	MOCVD	SiC	45 (fg)	16	6.7	14.4	-
[10]	MOCVD	SiC	45 (fg)	15	4.8	1 6.9	-
[11]	MOCVD	SiC	75 (fg)	14	5.16	27.7	6.8
[11]	MOCVD	SiC	75 (fg)	16	6.15	27.3	6.8
[11]	MOCVD	SiC	75 (fg)	18	7.02	27.1	6.8
[11]	MOCVD	SiC	75 (fg)	20	7.94	26.9	6.8

Table 2.3.2: small-signal metrics for N-polar HEMTs published between 2007-2018. Note: L_g is the gate length, 'fg' stands for foot-gate (bottom part of deep-recess gate.

Ref	Growth technique	Sub.	$G_{m(peak)}$ (mS/mm)	V_{ds} (volts)	f_T (Hz)	f_{max} (Hz)	Lg (nm)
[12]	MBE	SiC	195	10	18	44	700
[12]	MBE	SiC	-	-	17	36	700
[12]	MBE	SiC	-	-	14	35	700
[2]	MBE	SiC	133	-	24	44	700
[3]	MBE	SiC		-	17	37	700
[4]	MBE	SiC	200	-	17	58	600
[4]	MBE	SiC	200	-	17	58	600
[5]	MBE	SiC	200	15	17	65	700
[6]	MOCVD	Al2O3	130	8	16	40	700
[6]	MOCVD	Al2O3	130	8	16	40	700
[7]	MOCVD	SiC	230	-40	16	58	700
[7]	MOCVD	SiC	230	-40	16	58	700
[7]	MOCVD	SiC	230	-40	16	58	700
[13]	MBE	SiC	1000	2	155	20	30
[13]	MBE	SiC	1105	2	155	20	60
[14]	MOCVD	Al2O3	-	-	343	351	80
[8]	MOCVD	Al2O3	695	5	149	330	60 (fg)
[8]	MOCVD	Al2O3	695	5	149	330	60 (fg)
[9]	MOCVD	Al2O3	620	5	149	276	70 (fg)
[9]	MOCVD	Al2O3	620	5	149	276	70 (fg)
[10]	MOCVD	SiC	-	-	112	323	45 (fg)
[10]	MOCVD	SiC	-	-	112	323	45 (fg)
[15]	MOCVD	SiC	326	5	93	313	50
[11]	MOCVD	SiC	460	5	113	238	75 (fg)
[11]	MOCVD	SiC	460	5	113	238	75 (fg)
[11]	MOCVD	SiC	460	5	113	238	75 (fg)
[11]	MOCVD	SiC	460	5	113	238	75 (fg)

Early HEMT technology grown by MBE (2007-2010):

One of the first N-polar GaN HEMTs was grown and developed by Rajan et al. in 2007 and consisted of a GaN/AlGaN:Si/AlGaN/GaN structure grown on C-face SiC by MBE with a planar gate and alloyed source and drain contacts [12]. Although hall data of the original HEMT structure revealed a sheet charge and mobility of $1 \times 10^{13} cm^{-2}$ and 1400 $cm^2 V^{-1} s^{-1}$ respectively, when the device was modified to reduce dispersion and gate leakage (explained further on) charge and mobility dropped to $6 \times 10^{12} cm^{-2}$ and 1200 $cm^2 V^{-1} s^{-1}$ respectively [12]. This was much lower than state-of-the-art Ga-polar devices of the time which were reporting mobilities in excess of 2000 $cm^2 V^{-1} s^{-1}$ [16]. In the early development of N-polar GaN HEMTs it was found that given a significantly thick AlGaN back-barrier or thin AlN back-barrier, both of which were needed to produce a 2DEG channel, a positive sheet charge was induced at the back GaN/AlGaN interface - an effect which is illustrated in the band-diagram shown in Fig. 2.3.1 below. This parallel channel was found to come from a donor state that existed 60 meV above the valence band at the GaN/AlGaN interface [17]. It was found that this parallel channel, known as the negatively polarized interface (NPI) [17], could be suppressed by doping the thin region of the GaN directly below the backbarrier and by grading the AlGaN backbarrier thereby pulling the Fermi-level away from the donor state. This effect of this 10 nm Si-doped GaN layer below the back-barrier is illustrated in Fig. 2.3.1 [12], [17]. Small-signal measurements of this early HEMT yielded a f_T and f_{max} of 14 and 35 GHz respectively [17] which were significantly lower than reported Ga-polar devise of the time [18].

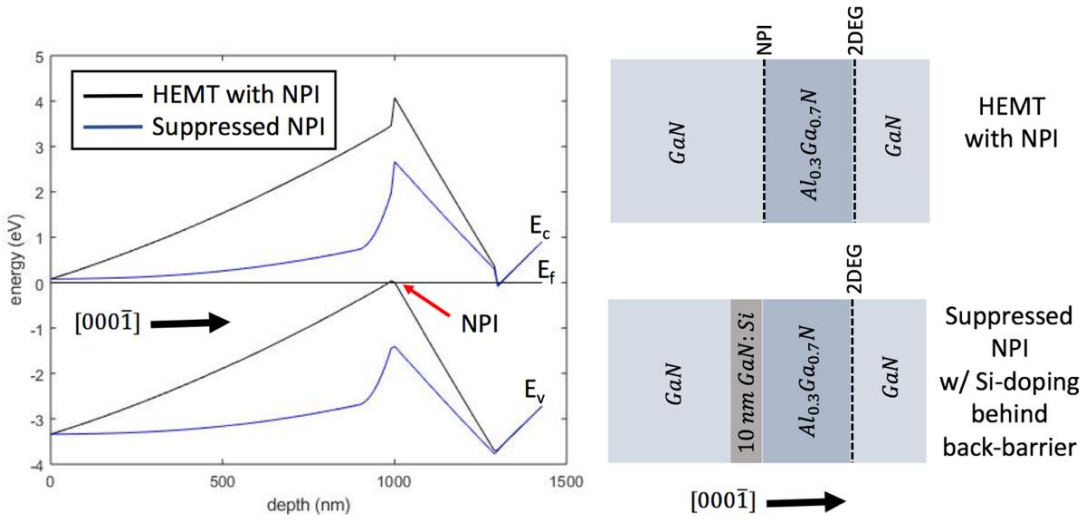

Figure 2.3.1: Band-diagram showing the NPI and suppression of the NPI via. Si-doping behind back-barrier (left). Corresponding device structures (right). This structure was similar to what was published by Rajan et al. in 2007 [12].

Later in 2007 Wong et el. published his work on an N-face GaN HEMTs which utilized a non-alloy back-barrier to reduce alloy scattering and utilized SiN passivation on the device surface which greatly reduce DC-RF dispersion and improving mobility. HEMT epi was again grown by MBE on a SiC substrate, however, instead of using an AlGaN backbarrier, an 12x AlN/GaN superlattice was used to induce the same kind of polarization in which the 30% AlGaN back-barrier used in previous work which. It was believed that this 12x SL back-barrier would yield a 2DEG which had considerably lower alloy-scattering. This 'digital-AlGaN backbarrier', a name dubbed by the author, plus a 4 nm GaN spacer separating the channel from the digital back-barrier used to further separate the channel from the Si-doped GaN behind the back-barrier, yielded a maximum hall mobility of 1750 $cm^2V^{-1}s^{-1}$ and a sheet charge of $7 \times 10^{12} cm^{-2}$ [2]. The device architecture and band-diagram are shown in figure 2.3.2 below. This was a 20% improvement in mobility when

compared with previous work. This device was also the first reported N-polar device where large-signal measurements were acquired using load-pull [2]. Measured at 4 GHz and at a drain bias of 40 V this device displayed a transducer gain G_T of 10.3 dB, a maximum power output density P_o of 4.5 W/mm and a PAE of 34%. DC and pulsed-IV measurements showed a significant decrease in current collapse for the device passivated by MOCVD SiN_x [2]. SiN_x passivation has been a common method of reducing gate-lag by neutralizing surface traps in GaN; without passivation surface traps slow down the time it takes for the gate to modulate the 2DEG channel thereby causing current collapse at higher frequencies [19]. Similar work done by Wong et al. in 2008 which utilized a single thin AlN back-barrier and a dual AlN back-barrier design were grown by MBE and processed [3], [20]. At 4 GHz these MBE-grown devices yielded a PAE of 58% and 67%, a P_{out} of 7.1 and 6.4 W/mm at a V_d of 35 V and 28 V respectively with a highest PAE of 71% reported in the dual-AlN backbarrier device [3], [20]. f_T and f_{max} for the dual AlN back-barrier was found to be 17 GHz and 58 GHz respectively at I_{ds}=460 mA/mm and a V_{ds}=20 V [20]. Utilizing the single AlN backbarrier design, Mishra et al. reported a P_{out} of 8.1 w/mm at V_d = 40 V with an associated PAE of 54% in 2010 [21].

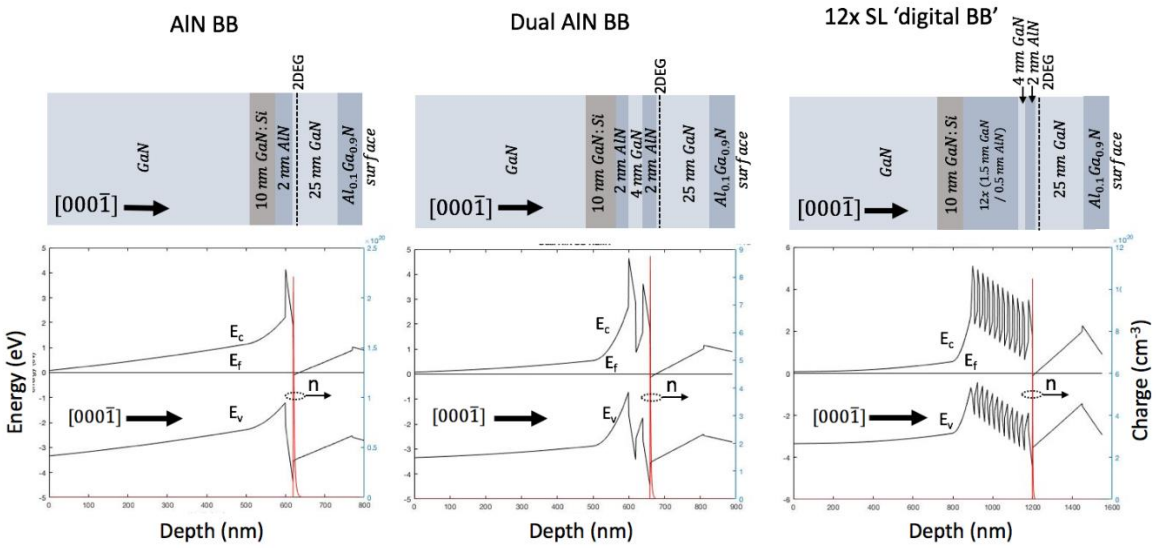

Figure 2.3.2 band diagram and device structure for: (Left) single AlN back-barrier HEMT similar to that done in [3]. (middle) dual AlN back-barrier HEMT similar to that done in [3]. (right) 12x digital AlGaN back-barrier HEMT similar to that done in [2].

MOCVD grown N-polar HEMT Technology (2007-2018):

While N-polar GaN HEMTs grown by MBE were showing continual improvements in device performance from 2007-2010, high-quality N-polar GaN films grown by MOCVD had already been reported as early as 2007 [22], [23]. Early reports of N-polar GaN grown by MOCVD revealed hexagonal hillox on the surface which were attributed to inversion domains [24]. It was discovered that these hillox could be suppressed and smooth surface morphology could be achieved in N-polar GaN grown by MOCVD by using miscut substrates. Keller et al. demonstrated that growing on a sapphire substrate with a 2^o miscut from the m-plane which yielded more periodic steps with shorter terrace-widths, eliminated hillox from the surface [22]. The same effect was also demonstrated on SiC substrates [25]. Using thicker MOCVD GaN buffer layers, typically on the order of a few microns, the amount of vertically propagating TDs seen on the film surface could be dramatically reduced.

Whereas MBE grown GaN on SiC yielded a TDD on the order of 1e10 cm^{-2} [26], the GaN surface of thick MOCVD grown buffers was on the order of 1e8 cm^{-2} [25]. MOCVD grown HEMT structures were not only an improvement in terms of mobility, which would otherwise be impeded by dislocation density, but also led to devices with higher breakdown fields due to the thick GaN buffers layer which was realized by MOCVD [37].

In 2011 Kolluri et al. presented an N-polar HEMT grown by MOCVD on a miscut sapphire substrate which yielded an output power density of 12.1 W/mm at 4 GHz at a drain bias of 50 V and a channel breakdown voltage of 170 V [6]. At the time this was the highest power density reported for an N-polar device. Kolluri's novel device structure, which is illustrated in figure 2.3.3 below, employed a Si-doped graded AlGaN layer behind the main AlGaN backbarrier further suppressing any NPI which might be generated as the gate was biased [6]. Unfortunately, self-heating of the sapphire substrate led to degradation in I_{DS} for higher DC source-drain voltages [6], an effect which had been observed in earlier Ga-polar devices grown by MBE [26]. This effect of self-heating, however, can be easily remedied by switching to a substrate with better thermal conductivity such as SiC. This is precisely what Kolluri et al. did in 2012 [7]. In addition to fixing the problem of self-heating by switching to a SiC substrate, this device also featured a 0.7 nm AlN interlayer between the GaN channel and the $Al_{.38}Ga_{.62}N$ backbarrier. This AlN interlayer provided additional polarization charge which led to higher 2DEG charge and pushed the 2DEG further away from the back-barrier/channel interface thereby reducing the effects of random alloy scattering [7], [27], a problem which will be shown to be a major factor in degrading 2DEG mobility [28]. These seemingly subtle improvements led to a device with P_{out} of 20.7 W/mm at 4 GHz [7], a 42% improvement compared with the previous device [6]. This particular

device reported the highest X-band power density for an N-polar device and was on-par with state-of-the-art Ga-polar devices of that time [7].

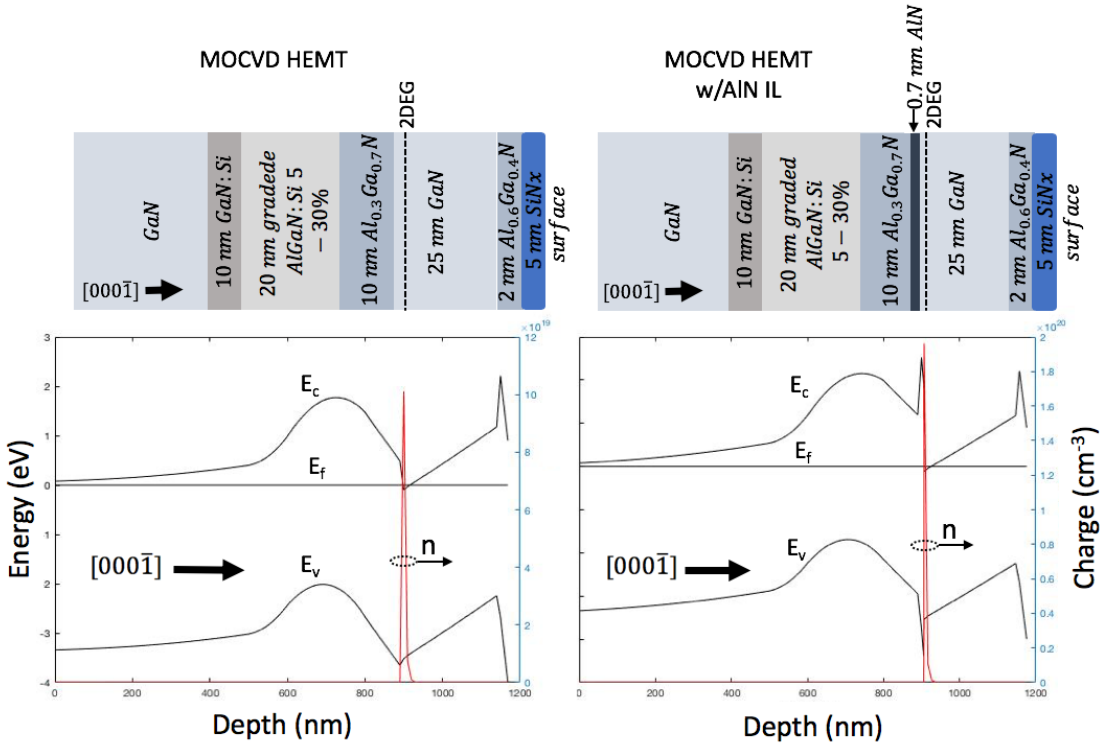

Figure 2.3.3: device structure (top) and band-diagram (bottom) for MOCVD grown HEMTs with graded AlGaN back-barrier (left), and the same structure but with a 0.7 nm AlN interlayer (right), similar to that done in [6] and [7] respectively.

The N-polar devices demonstrated by Kolluri et at. utilized alloyed ohmic contacts for the source and drain [6], [7] which were limited in terms of the contact resistance and sheet resistance made between the source/drain contacts and the 2DEG channel. In 2010 it was demonstrated by Dasgupta et al. that using an MBE regrown graded InGaN layer for the source and drain contacts yielded a contact resistance of 27 Ω-μm [29]. In 2012 it was demonstrated by Meyer et al. that a contact resistance of 80 Ω -μm was achieved when using MBE n+ regrown source and drain contacts for N-polar HEMTs [30].

In an effort push N-polar HEMT technology to a point where it could compete with Ga-polar devices in terms of f_{max}, Denninghoff et al. made a device in 2012 using the aforementioned MBE n+ regrowth technology [14]. This device also made use of a 1.1- μm tall T-gate - a method widely used in Ga-polar GaN HEMT technology to reduce gate-to-drain capacitance (C_{gd}) and minimize gate resistance (R_g) [36]. Fig. 2.3.5 below shows a simplified version of the T-Gate and regrown ohmic device architecture. Denninghoff's device exhibited an f_{max} of 351-GHz at a V_{DS} of 8 V which was higher than any other N-polar device at that time and was comparable to what had been observed in top Ga-polar devices [14]. Later in 2013 Denninghoff reported a device with an f_{max} of 405 GHz and an f_T of 204 GHz at a V_{DS} = 8 V [35]. In 2018 using the same T-gate and regrown S/D ohmic contact method, Zhang et al. made a device with a f_{max} of 313 GHz at a V_{DS} of 26 V by increasing thickness of the SiN passivation layer to extend beyond the gate [15].

Deep Recess Gate Technology:

While N-polar HEMT technology was making significant progress in the X-band and C-band frequency range, dispersion in the form of current collapse at high frequencies was limiting it's movement into higher frequency bands. In 2001 Vetury et al. demonstrated how surface states between the gate and drain contacts in Ga-polar HEMTs led to a 'virtual gate' (VG) over the channel between the gate and drain [31]. Fig. 2.3.4 below illustrates the concept of the virtual gate in an N-polar device. When a HEMT amplifier biased in class A mode moves up and down the load line the charge under the virtual gate (channel region between the gate and the drain – closer to the gate) will respond slower to V_g with respect to the charge directly underneath the gate. This is because the time it takes for surface trap

states to respond to an applied bias is dependent on some time constant, T_{TRAP}, which is typically much longer than the time it takes to generate or deplete the 2DEG under a gate [31], [32]. Passivating surface states by capping the device structure with SiN_x [7] [8] [15][16][21] [33] [15] or Al_2O_3 [34] had already been practiced with some success. In addition to dielectric passivation, field-platting in higher power devices has also been shown to reduce the effects of these surface states [33]. Unfortunately, field-platting and surface passivation using thick dielectric layers introduces parasitic capacitances which make these devices incapable of performing at higher frequencies.

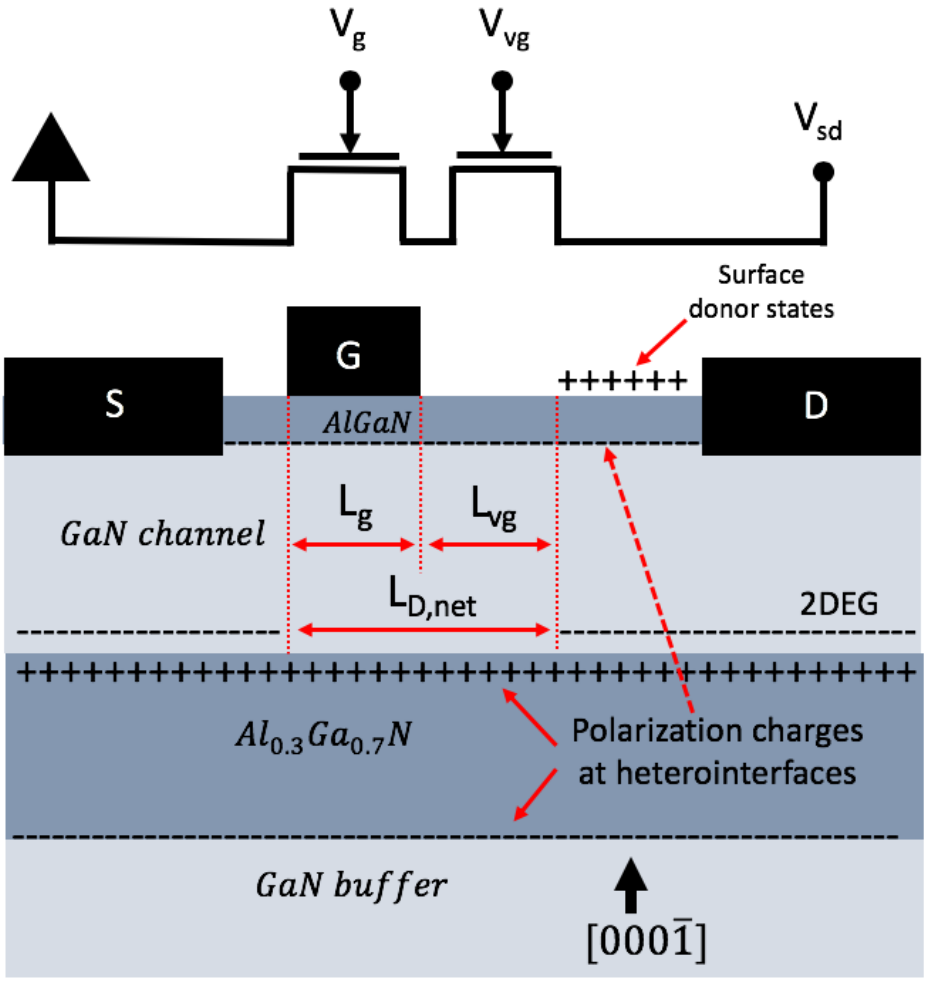

Fig. 2.3.4: illustration of the virtual gate effect for an N-polar HEMT

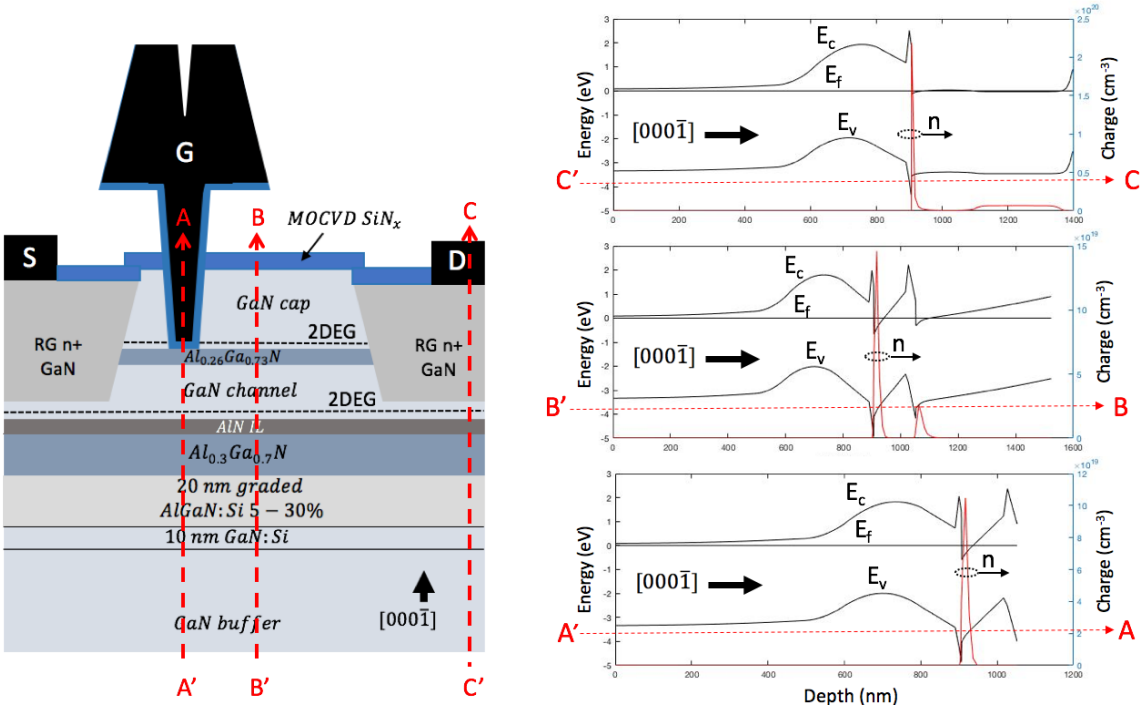

Fig. 2.3.5: Deep recessed (DR) HEMT architecture (left) and corresponding band diagrams for the gate-region, channel-region and ohmic-contact region (right – bottom to top respectively)

Instead of field-platting or improving dielectric passivation to neutralize surface states it was realized that for N-polar structures one could simply grow an additional AlGaN/GaN layer on top of the GaN channel creating a parallel channel which would image the positively charged surface states. Etching through a region of the top GaN cap for T-gate deposition ensured the gate only controlled the 2DEG channel closest to the GaN/AlGaN backbarrier and not the parallel channel created by the GaN cap. This deep recess gate technology was first used for an N-polar HEMT in 2016 by Wienecke et al. [9]. An illustration of the deep-recessed gate device is shown in Fig. 2.3.5 above. Using the deep-recessed gate Wienecke at al achieved an f_{max}/f_T of 276/149 GHz, but more importantly, this device exhibited a P_o of 2.9 W/mm at 94 GHz for a V_{DS} = 10 V which was comparable to some of the best performing Ga-polar devices of that time [9]. Also in 2016, a P_o of 4.2

W/mm at 94 GHz was achieved using a self-aligned recessed gate by Romanczyk at al. [8]. Where the devices in [8] and [9] were both grown by MOCVD on sapphire substrates the same deep-recess gate method used in [9] was used again in 2017 on a SiC substrate; this time a P_o of 6.5 W/mm was achieved at 94 GHz [10] – more than double of what it had been on a sapphire substrate a year before [9]. Finally, in 2018 a P_o of 8 W/mm was achieved at 94 GHz using the self-aligned gate-recess process similar to what was used in [8] for HEMT epi grown on a SiC substrate [11]. For this device it was also shown that the same P_o of 8 W/mm was maintained at 10, 30 and 94 GHz indicating its efficiency across a range of frequencies [11].

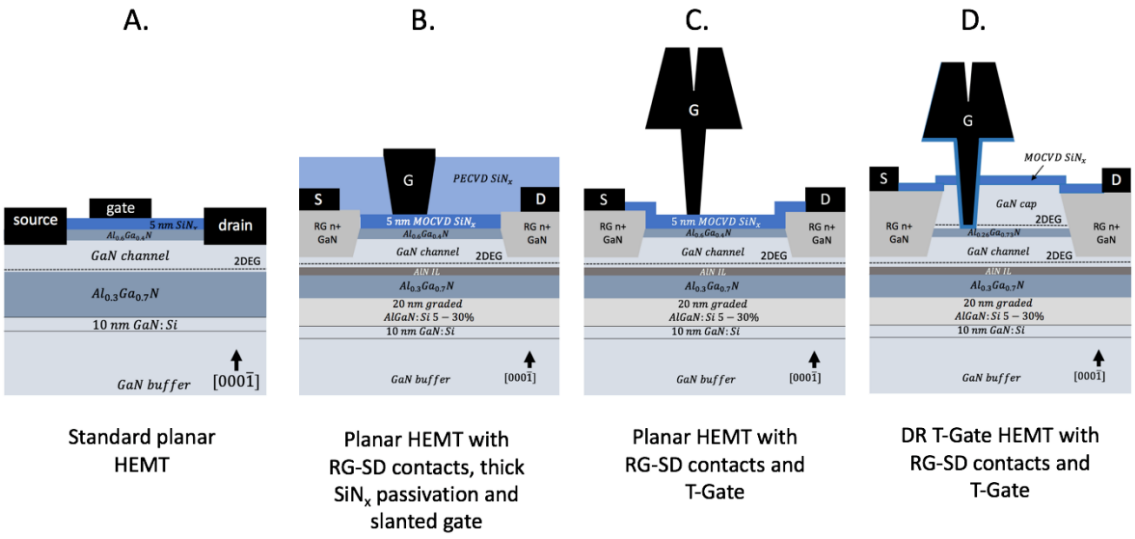

Figure 2.3.6: Evolution of N-polar device architecture. A-D (left to right). A. Standard planar HEMT architecture. B. Planar HEMT with regrown (RG) source-drain (SD) contacts, thick SiN_x passivation and slanted gate. C. Planar HEMT with RG-SD contacts and T-gate. D. Deep-recessed HEMT with T-gate and RG-SD contacts.

2.4 Conclusion:

It was the purpose of this chapter to inform the reader of the exceptional progress made in N-polar HEMT technology in the past decade. A brief history of N-polar technology was presented and it was shown that current N-polar HEMTs have surpassed Ga-polar HEMTs in terms of large signal device performance. This is by no means a comprehensive history of N-polar technology; more in-depth information on this can be found in [1], [17], [25]. With heteroepitaxially grown N-polar GaN HEMTs showing such spectacular performance it begs the question as to what possible improvements could be made which might push N-polar technology to the next level. This history of N-polar HEMT technology is intended to serve as a segue to the following chapter which will present the motivation for investigating N-polar HEMTs grown on bulk GaN by MBE which will hopefully push N-polar HEMT metrics beyond their current reported values.

References:

[1] M. Guidry, Thesis (2018)

[2] M. H. Wong *et al.*, "N-face high electron mobility transistors with a GaN-spacer," *Phys. Status Solidi A*, vol. 204, no. 6, pp. 2049–2053, Jun. 2007.

[3] Man Hoi Wong *et al.*, "N-Face Metal–Insulator–Semiconductor High-Electron-Mobility Transistors With AlN Back-Barrier," *IEEE Electron Device Lett.*, vol. 29, no. 10, pp. 1101–1104, Oct. 2008.

[4] M. H. Wong, Y. Pei, J. S. Speck, and U. K. Mishra, "High power N-face GaN high electron mobility transistors grown by molecular beam epitaxy with optimization of AlN nucleation," *Appl. Phys. Lett.*, vol. 94, no. 18, p. 182103, May 2009.

[5] M. H. Wong *et al.*, "X-band power performance of N-face GaN MIS-HEMTs," *Electron. Lett.*, vol. 47, no. 3, p. 214, 2011.

[6] S. Kolluri, S. Keller, S. P. DenBaars, and U. K. Mishra, "N-Polar GaN MIS-HEMTs With a 12.1-W/mm Continuous-Wave Output Power Density at 4 GHz on Sapphire Substrate," *IEEE Electron Device Lett.*, vol. 32, no. 5, pp. 635–637, May 2011.

[7] S. Kolluri, S. Keller, S. P. DenBaars, and U. K. Mishra, "Microwave Power Performance N-Polar GaN MISHEMTs Grown by MOCVD on SiC Substrates Using an Al2O3 Etch-Stop Technology," *IEEE Electron Device Lett.*, vol. 33, no. 1, pp. 44–46, Jan. 2012.

[8] B. Romanczyk *et al.*, "mm-Wave N-polar GaN MISHEMT with a self-aligned recessed gate exhibiting record 4.2 W/mm at 94 GHz on Sapphire," in *2016 74th Annual Device Research Conference (DRC)*, Newark, DE, USA, 2016, pp. 1–2.

[9] S. Wienecke *et al.*, "N-Polar Deep Recess MISHEMTs with Record 2.9 W/mm at 94 GHz," *IEEE Electron Device Lett.*, pp. 1–1, 2016.

[10] S. Wienecke *et al.*, "N-Polar GaN Cap MISHEMT With Record Power Density Exceeding 6.5 W/mm at 94 GHz," *IEEE Electron Device Lett.*, vol. 38, no. 3, pp. 359–362, Mar. 2017.

[11] B. Romanczyk *et al.*, "Demonstration of Constant 8 W/mm Power Density at 10, 30, and 94 GHz in State-of-the-Art Millimeter-Wave N-Polar GaN MISHEMTs," *IEEE Trans. Electron Devices*, vol. 65, no. 1, pp. 45–50, Jan. 2018.

[12] S. Rajan, A. Chini, M. H. Wong, J. S. Speck, and U. K. Mishra, "N-polar GaN/AlGaN/GaN high electron mobility transistors," *J. Appl. Phys.*, vol. 102, no. 4, p. 044501, Aug. 2007.

[13] Nidhi, S. Dasgupta, J. Lu, J. S. Speck, and U. K. Mishra, "Self-Aligned N-Polar GaN/InAlN MIS-HEMTs With Record Extrinsic Transconductance of 1105 mS/mm," *IEEE Electron Device Lett.*, vol. 33, no. 6, pp. 794–796, Jun. 2012.

[14] D. J. Denninghoff, S. Dasgupta, J. Lu, S. Keller, and U. K. Mishra, "Design of High-Aspect-Ratio T-Gates on N-Polar GaN/AlGaN MIS-HEMTs for High $f_{\max}$," *IEEE Electron Device Lett.*, vol. 33, no. 6, pp. 785–787, Jun. 2012.

[15] X. Zheng *et al.*, "Analysis of MOCVD SiNx Passivated N-Polar GaN MIS-HEMTs on Sapphire With High $f_{max}\cdot V_{DS,Q}$," *IEEE Electron Device Lett.*, vol. 39, no. 3, pp. 409–412, Mar. 2018.

[16] U. K. Mishra, Shen Likun, T. E. Kazior, and Yi-Feng Wu, "GaN-Based RF Power Devices and Amplifiers," *Proc. IEEE*, vol. 96, no. 2, pp. 287–305, Feb. 2008.

[17] M. H. Wong *et al.*, "N-polar GaN epitaxy and high electron mobility transistors," *Semicond. Sci. Technol.*, vol. 28, no. 7, p. 074009, Jul. 2013.

[18] T. Palacios, A. Chakraborty, S. Heikman, S. Keller, S. P. DenBaars, and U. K. Mishra, "AlGaN/GaN high electron mobility transistors with InGaN back-barriers," *IEEE Electron Device Lett.*, vol. 27, no. 1, pp. 13–15, Jan. 2006.

[19] Hyungtak Kim, R. M. Thompson, V. Tilak, T. R. Prunty, J. R. Shealy, and L. F. Eastman, "Effects of SiN passivation and high-electric field on AlGaN-GaN HFET degradation," *IEEE Electron Device Lett.*, vol. 24, no. 7, pp. 421–423, Jul. 2003.

[20] Man Hoi Wong, Yi Pei, D. F. Brown, S. Keller, J. S. Speck, and U. K. Mishra, "High-Performance N-Face GaN Microwave MIS-HEMTs With > 70% Power-Added Efficiency," *IEEE Electron Device Lett.*, vol. 30, no. 8, pp. 802–804, Aug. 2009.

[21] U. K. Mishra *et al.*, "N-polar GaN-based MIS-HEMTs for mixed signal applications," in *2010 IEEE MTT-S International Microwave Symposium*, Anaheim, CA, USA, 2010, pp. 1130–1133.

[22] S. Keller *et al.*, "Influence of the substrate misorientation on the properties of N-polar GaN films grown by metal organic chemical vapor deposition," *J. Appl. Phys.*, vol. 102, no. 8, p. 083546, Oct. 2007.

[23] S. Keller *et al.*, "Recent progress in metal-organic chemical vapor deposition of (000-1) N-polar group-III nitrides," *Semicond. Sci. Technol.*, vol. 29, no. 11, p. 113001, Nov. 2014.

[24] J. L. Weyher *et al.*, "Morphological and structural characteristics of homoepitaxial GaN grown by metalorganic chemical vapour deposition (MOCVD)," *J. Cryst. Growth*, vol. 204, no. 4, pp. 419–428, Aug. 1999.
[25] S. Keller *et al.*, "Recent progress in metal-organic chemical vapor deposition of (000-1) N-polar group-III nitrides," *Semicond. Sci. Technol.*, vol. 29, no. 11, p. 113001, Nov. 2014.
[26] S. W. Kaun, M. H. Wong, U. K. Mishra, and J. S. Speck, "Molecular beam epitaxy for high-performance Ga-face GaN electron devices," *Semicond. Sci. Technol.*, vol. 28, no. 7, p. 074001, Jul. 2013.
[27] S. Kolluri *et al.*, "Influence of AlN interlayer on the anisotropic electron mobility and the device characteristics of N-polar AlGaN/GaN metal-insulator-semiconductor-high electron mobility transistors grown on vicinal substrates," *J. Appl. Phys.*, vol. 108, no. 7, p. 074502, Oct. 2010.
[28] E. Ahmadi, "Growth Optimization of III-N Electronic Devices by Plasma-Assisted Molecular Beam Epitaxy," p. 146.
[29] S. Dasgupta *et al.*, "Ultralow nonalloyed Ohmic contact resistance to self aligned N-polar GaN high electron mobility transistors by In(Ga)N regrowth," *Appl. Phys. Lett.*, vol. 96, no. 14, p. 143504, Apr. 2010.
[30] D. J. Meyer *et al.*, "N-polar n+ GaN cap development for low ohmic contact resistance to inverted HEMTs," *Phys. Status Solidi C*, vol. 9, no. 3–4, pp. 894–897, Mar. 2012.
[31] R. Vetury, N. Q. Zhang, S. Keller, and U. K. Mishra, "The impact of surface states on the DC and RF characteristics of AlGaN/GaN HFETs," *IEEE Trans. Electron Devices*, vol. 48, no. 3, pp. 560–566, Mar. 2001.
[32] S. C. Binari *et al.*, "Trapping effects and microwave power performance in AlGaN/GaN HEMTs," *IEEE Trans. Electron Devices*, vol. 48, no. 3, pp. 465–471, Mar. 2001.
[33] O. S. Koksaldi *et al.*, "N-Polar GaN HEMTs Exhibiting Record Breakdown Voltage Over 2000 V and Low Dynamic On-Resistance," *IEEE Electron Device Lett.*, vol. 39, no. 7, pp. 1014–1017, Jul. 2018.
[34] T. Hashizume, S. Ootomo, T. Inagaki, and H. Hasegawa, "Surface passivation of GaN and GaN/AlGaN heterostructures by dielectric films and its application to insulated-gate heterostructure transistors," *J. Vac. Sci. Technol. B Microelectron. Nanometer Struct.*, vol. 21, no. 4, p. 1828, 2003.
[35] D. Denninghoff, J. Lu, E. Ahmadi, S. Keller, and U. K. Mishra, "N-polar GaN/InAlN/AlGaN MIS-HEMTs with 1.89 S/mm extrinsic transconductance, 4 A/mm drain current, 204 GHz fT and 405 GHz fmax," in Proc. 71st Device Res. Conf. (DRC), Santa Barbara, CA, USA, Jun. 2013, pp. 197–198, doi: 10.1109/DRC.2013.6633861.
[36] O. Breitschadel, H. Grabeldinger, B. Kuhn, F. Scholz, W. Walthers, M. Berroth, I. Daumiller, K. B. Schad, E. Kohn, H. Schweizer, "Short-channel AlGaN/GaN HEMTs with 70 nm T-gate," Elect. Letters, vol. 35 iss. 23, pp. 2019-2019, Nov. 1999.
[37] C. Gupta, Y. Enatsu, G. Gupta, S. Keller, and U. K. Mishra, "High breakdown voltage p-n diodes on GaN on sapphire by MOCVD: High breakdown voltage p-n diodes," *Phys. Status Solidi A*, vol. 213, no. 4, pp. 878–882, Apr. 2016.

Chapter 3: Motivation for homoepitaxially MBE-grown GaN devices on bulk-GaN

3.1 Introduction:

Given the success which N-polar HEMTs grown on by MOCVD have displayed [1]–[3] when compared to past N-polar devices grown by MBE [4], [5] there may exist some skepticism about a return to MBE grown devices. Furthermore, when considering the high cost and low abundance of bulk GaN substrates there may be an even greater misgiving to pursue homoepitaxially grown devices. It is the purpose of this chapter to answer two important questions: first, what is the motivation for homoepitaxially grown devices, and second, what advantages could MBE-grown devices have over MOCVD grown devices. In will be shown that the interest in homoepitaxy comes from film quality whereas the interest in pursuing MBE over MOCVD has to do with versatility in device architecture, particularly in MBE's ability to grow thick coherently-strained AlN interlayers. GaN films grown on foreign substrates such as SiC, Si and sapphire exhibit a high density of dislocations generated by thermal and lattice mismatch. The evidence presented in this chapter suggests that these dislocations act as scattering centers which lower device performance. In that case, these dislocation-related scattering centers can lead to undesired power dissipation for devices biased in deep class-A mode where a large source-drain current is present. Growing on bulk GaN substrates as oppose to foreign substrates results in films with more than an order of magnitude lower dislocation density. Furthermore, it will be shown that alloy scattering is the chief factor limiting mobility in the 2DEG channel. MBE has the advantage of being able to produce ultra-thick fully strained AlN backbarriers which results in a channel with higher charge and, more importantly, greatly reduces the effects of alloy scattering.

This chapter is laid out as such: first, there will be a brief summary discussing the basics of plasma-based MBE and why Ga-rich growth is favorable to N-rich growth for the typical growth temperatures used by MBE. Next, the motivation for pursuing homoepitaxy will be given through a discussion of dislocation related scattering which will be followed by a synopsis on alloy-scattering and this can be mitigated by MBE.

3.2 PAMBE of N-face GaN:

PAMBE

What separates plasma-assisted MBE from conventional MBE is how gas sources such as N_2 or O_2 are converted from the diatomic gas phase to active species – how the diatomic bonds a cracked. In a standard GaAs based MBE system all of the source materials (i.e. Ga, Al, In and As) are contained in effusion cells where the beam flux is controlled by the cell temperature. Increasing the cell temperature increases the partial pressure of the source material exponentially thereby increasing the beam-equivalent-pressure (BEP) of the source material leaving the cell [6]. The ultra-low background chamber pressure in MBE, typically 1e-10 – 1e-8 Torr, enables the active species to travel from the opening of the effusion cell to the sample surface unimpeded. Thus the measured BEP at the cell opening and the sample surface should be the same. This technique works well for solid and liquid phase source materials such as Ga, Al and In, however, gas-phase precursors such as N_2 and O_2 require significantly higher energy to decompose.

N_2 gas has a triple with an associated bond energy of 942 kJ mol^{-1} (~9.79 eV/bond) [7]. It has been demonstrated, by using filament heating, that a filament temperature of over 3500 K is required to dissociate just 5% of N_2 [8]; this is significantly higher than the typical

growth temperatures of MBE (300^o - 900^o C.). Hence some source of energy other than temperature is required to dissociate diatomic gases such as N_2. A common method of cracking the N_2 triple-bond is by using an RF-plasma. Although this work attempt to discuss the basics of plasma-enhanced dissociation of inert gases, a more in-depth explanation of how plasma systems work can be found in [6], [9]. A simplified version of an RF plasma network consists of two electrodes connected to a RF power supply and a matching network. The gas between the two electrodes is electrically insulating until a high voltage source, typically a large capacitor, supplies enough voltage to breakdown the gas and create an arc between the two electrodes. When this happens a fraction of the gas ionizes and the positively charged ions accelerate toward the cathode where they collide creating more electrons which then accelerate toward the anode. As these traveling electrons collide inelastically with more gas species they create more ions. The RF-field (typically 13.56 MHz) between the two plates prevents the accumulation of charge on either plate which would otherwise reduce the electric field until the plasma extinguishes. At high enough frequencies, the slow-moving ions cannot follow the changing electric field compared to the fast-moving electronics which continue to collide with either electrode creating more and more ions by continuing to collide with the gas species. To eliminate power loss from mismatch, a matching network must be used to ensure the impedance-matching [50]. Figure 3.2.1 gives a very fundamental illustration of a RF plasma source commonly used in PAMBE.

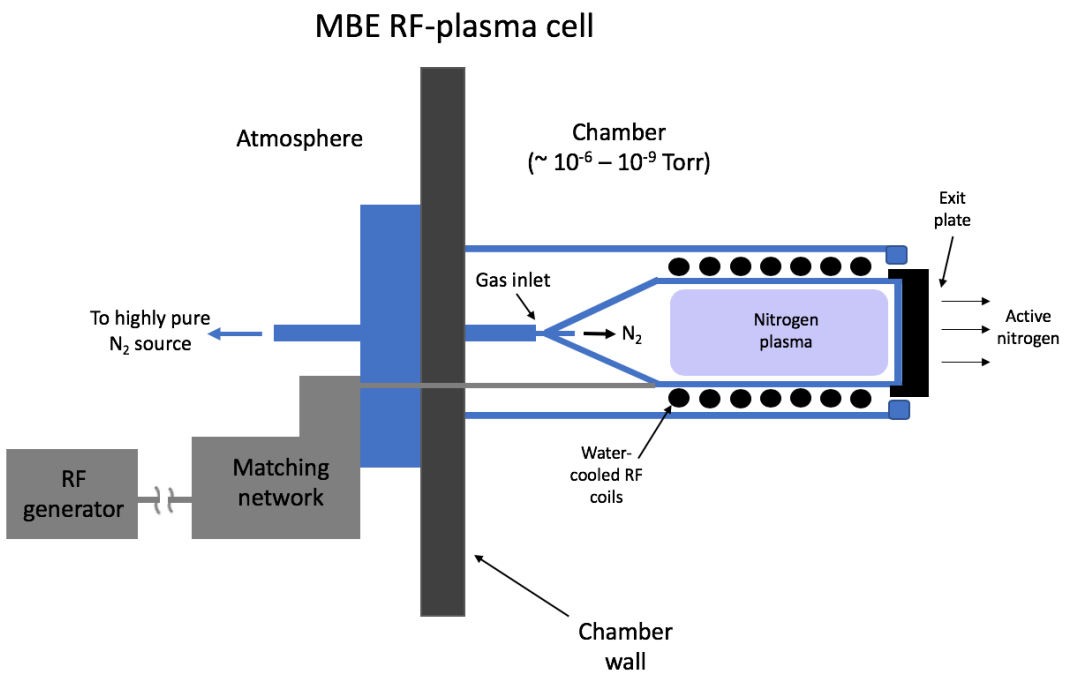

Figure 3.2.1: simplified version of RF plasma cell commonly used in PAMBE

Employing an RF plasma source is the most common method of creating active nitrogen in MBE grown GaN. NH_3-MBE has also been used extensively for growth of MBE nitrides [10]. Gas-phase MBE such as NH_3-MBE is similar to MOCVD where NH_3 molecules undergo pyrolysis near the sample surface where temperatures exceed 800^o C. For this thesis, the focus will primarily be on PAMBE of GaN however more information on NH_3 MBE can be found in [11][10].

Ga-Rich growth:

Unlike MBE, MOCVD nitride semiconductors are typically grown at temperatures of 1000^o C. or higher under N-rich conditions. These high growth temperatures give rise to high adatom motilities on the surface which reduce the probability of island-nucleation and

promote step-flow growth. MBE grown nitrides, on the other hand, our typically growth between 500^{o} and 800^{o} C [10]–[13]. Growing at these low temperatures greatly reduces the adatom mobility leading to rough 3D surfaces as was demonstrated by Tarsa et al. in 1997; N-rich growth of GaN by MBE resulted in films with a columnar structures initiated by the formation of stacking faults [12]. The chief cause of poor surface morphology in N-rich MBE grown GaN has been traced to the high (1.3 eV) diffusion barrier for N on the bare Ga-terminated surface [14]. Because of this N-adatoms are orders of magnitude less mobile with respect to Ga-adatoms on the GaN surface [14]. Growing in a Ga-rich regime, however, has been shown to improve adatom mobility at the lower temperatures employed by MBE leading to smooth surface morphology [12], [14]–[18]. This is because in the case of Ga-rich growth excess Ga floats on the surface which lowers the adatom diffusion barrier for N under the Ga-adlayer. Thus, the Ga-adlayer acts as an auto-surfactant leading to what is called adlayer enhanced lateral diffusion (AELD) [17]. It has been demonstrated experimentally by Koblmuller et al. and Tarsa et al. that increasing Ga-flux for a series of growths led to a dramatic improvement in surface morphology [12], [19]. Furthermore it was also shown by photoluminescence measurements that increasing Ga-flux led to a suppression in the near-band edge luminescence peak, (around 2.2 eV) commonly seen in GaN [20]; a high density of stacking faults was observed for films grown under more N-rich conditions which was believed to be associated with the 2.2 eV luminescence peak [12]. Although too high a Ga-flux to N-flux ratio can lead to Ga-droplets on the surface it has been shown that at least two monolayers of Ga is needed on the surface to promote step-flow growth of Ga-face GaN by MBE [18]. Thus growing GaN in the Ga-rich regime by PAMBE improves both surface morphology and film quality.

Growth of N-face GaN is particularly challenging due to the nature of the N-face surface. Mentioned previously, theoretical calculations made for Ga-polar surfaces predict a much higher diffusion barrier for N compared to Ga - 1.4 eV and 0.4 eV, respectively [21]. The N-polar surface is particularly unstable due to its higher chemical reactivity when compared to the Ga-polar surface [22]. Because of this the N-polar surface has a 5x higher adatom diffusion barrier with respect to the Ga-terminated surface [14]. This leads to challenges in particular for epitaxy via MOCVD, using N-rich conditions, which were mitigated by growing at temperatures above 1000^{o} C on miscut substrates [23]–[25]. Unlike Ga-polar GaN, growth of N-face GaN by Ga-rich MBE must be performed with less than 1 ML of excess Ga on the surface to prevent accumulation of droplets [18]. As will be discussed in the following chapters, early work of N-face GaN grown on non-miscut bulk GaN by MBE exhibited a high density of surface-pits [26], [27]. A more detailed explanation of the nature of these surface-pits and how they were suppressed will be discussed in chapter 4. Maintaining less than a monolayer of excess Ga on the surface throughout a long growth is unrealistic, therefor, in many cases, N-polar GaN is typically grown in the droplet regime and growths are interrupted periodically to desorb excess Ga preventing droplet formation on the surface.

3.3 Negative effects of lattice mismatch related dislocations:

In the preceding chapter a brief history of N-polar HEMT technology for devices grown by MOCVD on foreign substrates was presented which concluded with showing current N-polar HEMT technology has already surpassed Ga-polar technology in many respects [1], [2]. Even more impressive is the fact that these devices performed exceptionally

well despite having a threading dislocation density (TDD) on the order of 10^8 cm^{-2} [19]. Therefor there exists some curiosity as to whether or not device performance could be improved from devices with an order of magnitude or more, lower, TDD – something which could be achieved by utilizing a native substrate. To better understand the motivation for switching to bulk-GaN substrates, which are tremendously expensive and far less abundant compared with SiC and sapphire, it is necessary to understand how dislocations arising from lattice mismatch can negatively affect device performance.

When growing GaN on sapphire a 14% in-plane lattice mismatch and a 34% thermal mismatch (mismatch between thermal expansion coefficients of GaN and sapphire) exists, which, when grown by MOCVD, leads to a TDD between 10^9-10^{10} cm^{-2} in the GaN immediately following the heterointerface [28]. For GaN grown on (111) Si the in-plane lattice mismatch is only 17%, however, the thermal mismatch is 115% [29]. GaN and SiC, on the other hand, has an in-plane lattice mismatch of just 3.4% [30] and thermal expansion coefficients which are much closer in value ($\alpha_{GaN} = 5.6 \times 10^{-6}/K, \alpha_{AlN} = 4.2 \times 10^{-6}/K, \alpha_{SiC} = 3.2 \times 10^{-6}/K$) [31]. The TDs which are generated as a result of heteroepitaxial lattice mismatch propagate in the growth direction and, in the case of thin layers, terminate on the surface [32]. It has been verified by TEM that a high density of screw locations exist near the heterointerface as well as edge dislocations that thread from the heterointerface to the surface for heteroepitaxially grown GaN [33]. TDD in GaN grown on sapphire and SiC has been suppressed by almost two orders of magnitude by growing thick MOCVD GaN buffer layers. When growing thick GaN buffers, typically around 3 μm, TDs tend to intersect as they travel in the growth direction resulting in the annihilation of one or both TDs [34].

By utilizing the thick MOCVD grown buffer, a TDD on the order of 10^8 cm^{-2} is achieved for heteroepitaxially grown GaN on sapphire and SiC [19].

Dislocations and scattering:

There is a considerable amount of evidence, shown both theoretically and experimentally, that dislocations in GaN impede electron mobility. Nils et al. developed a model, which was verified experimentally, showing that filled traps along a TD line act as coulombic scattering centers impeding bulk mobility [35]. In 1999 Look et al. developed a model using the Boltzmann transport equation for charged-dislocation-line scattering showing that edge dislocations are electrically active [28]. Later, in 2003, conductive atomic force microscopy (C-AFM) imaging and scanning kelvin probe microscopy was utilized to show potential variations on the GaN surface arose from negatively charged TDs and localized leakage paths associated with dislocations; it was shown that while metal-decorated pure screw dislocations were neutral, edge dislocations near the surface were negatively charged [36]. Using non-destructive double crystal x-ray diffraction (DCXRD) and temperature-dependent Hall, Zhao et al. demonstrated that bulk electron mobility and carrier concentration were effected by TDD; higher dislocation density led to lower mobility and higher background carrier concentration [37].

Experimental and theoretical data showing dislocation related scattering was compared by Kyle et al. It was predicted that dangling bonds associated with edge dislocations act as acceptor states which trap electrons thereby becoming negatively charged; again, a reduction in bulk mobility was seen for GaN with high TDD grown by NH_3 MBE [10]. From this, dislocation-depended mobility was derived assuming an ionized acceptor-

like trap exists at every c-lattice translation along an edge-type dislocation causing an electric field around the dislocation [10]. Dislocation-dependent mobility was then calculated from the Boltzmann equation and has found to be [10][28][38]:

$$\mu_{Dis} = \frac{\hbar^3(\varepsilon_0\varepsilon_s)^2c^2(1+8L_D^2m^*k_BT/\hbar^2)^{3/2}}{\rho_{TDD}q^3m^{*2}L_D^4f^2} \tag{3.1}$$

Where ρ_{TDD} is the dislocation density given by the product of the distance between the acceptor-like trap states along a TD and the dislocation density ($\rho_{TDD} = d_{DIS}[N_{DIS}]$). The Debye screening length L_D is given by [38]:

$$L_D = \sqrt{\frac{\varepsilon_0\varepsilon_s k_BT}{(q^2n')}} \tag{3.2}$$

Where n' is the effective charge screening the negatively charged TD core [10]. Using Matthiessen's rule the mobility in (1) could be applied to all other mobilities from different scattering mechanism to get a net mobility:

$$\frac{1}{\mu_{net}} = \sum\frac{1}{\mu_i} \tag{3.3}$$

By growing a series of samples by NH_3-MBE with different TDDs, Kyle et al. demonstrated temperature dependent bulk mobility which fell very much in line with equation (3.1) [10].

Other negative effects of dislocations:

Coulombic electron scattering is not the exclusive factor effecting device performance in high TDD GaN devices. Surface-terminated dislocations in MBE-grown GaN can lead to surface pinholes, spiral hillox and depressions [12], [26], [32] [19]. The

poor surface morphology resulting from these dislocations can make it difficult to process devices with ultra-small features and can lead to defects on the surface which could potentially effect RF performance. For metal-rich MBE growth, in particular, metal decorated TDs have been shown to act as vertically conductive paths leading to high reverse-bias leakage in GaN Schottky contacts and vertical devices [39][52].

Given that the lowest reported TDDs for MOCVD GaN grown on SiC and sapphire is on the order of $10^8\ cm^{-2}$ [19], there exists an interest in homoepotaxially grown GaN where no lattice mismatch exists and TDDs $\sim 10^6\ cm^{-2}$ can be realized. To date, commercially available bulk GaN substrates have reported TDDs as low as $10^5\ cm^{-2}$ [53] – three orders of magnitude lower than heteroepitaxially grown MOCVD GaN templates. It has already been demonstrated that Ga-polar homoepitaxially grown HEMTs display higher Hall mobilities and lower sheet resistances [39], [40]. Therefor it seems likely that N-polar HEMTs grown on bulk GaN should follow suit in terms of improved device performance.

3.4 Alloy scattering:

For HEMTs, a significant amount of scattering comes from alloy disorder. These random fluctuations in the lattice due to the non-periodic nature of alloys mean that an electron must undergo some change in momentum due to the potential of the impurity or defect (U) as it travels through the alloy. A change in momentum, $\Delta k = k' - k$, leads to electron scattering with some characteristic scattering time ($\tau_{scatter}$) [51][42]. Although scattering from dislocations does contribute to a loss in mobility, as was shown in the previous section, it has been shown by room-temperature hall measurements that dislocation related scattering is negligible when compared to random-alloy scattering in AlGaN/GaN

heterostructures [41]. The random distribution of Al and Ga on group-V sites in $Al_xGa_{1-x}N$ leads to a fluctuation in the crystal potential such that Bloch waves are no longer valid [42]. Using the 1D Poisson solver program, BandEng, and the Born approximation [43], [44] in 2015 Ahmadi modeled 2DEG mobility from alloy scattering in an N-polar HEMT channel as a function of channel thickness and gate-bias [42]. It was shown in this work that the effects of alloy scattering increased as a function of reverse gate bias and scaled channel thickness; that is, as the channel thickness, not to be confused with channel length (source-to-drain spacing), was reduced the 2DEG wave-function was pushed further in to the AlGaN back-barrier thereby intensifying the effects alloy scattering [42]. In this same work there was also a degradation in mobility as the gate voltage was increased [42].

An Al-composition of approximately 34% has been shown to produce optimum 2DEG charge density and mobility in GaN/AlGaN heterostructures [45]. For Al-compositions lower than 34% the channel barrier is too small such that the 2DEG wave-function leaks into the AlGaN barrier while Al-compositions higher than 34% lead to higher surface roughness from lattice mismatch which also impedes mobility [45]. Looking at the history of N-polar HEMT technology in chapter two a remarkable increase in device performance was achieved when a 0.7 nm AlN IL was inserted between the AlGaN backbarrier and the GaN channel. The AlN IL, with a significantly higher conduction band offset (ΔE_c), pushed the 2DEG further into the GaN channel reducing the effects of alloy scattering and improving electron confinement [46]. In later work, however, it was demonstrated that going to thicker AlN interlayers, grown by MOCVD, resulted in a loss of electron mobility [49]. To the best of our knowledge, however, this AlN-IL thickness study for HEMT structures has not been repeated by MBE. This would be particularly interesting

given that MBE grown films have shown to produce thicker AlN interlayers coherently strained to GaN when compared to MOCVD grown structures [47], [48]. It will be shown in chapter four using HR-XRD and off-axis RSMs that AlN layers as thick as 8 nm were grown and remained coherently strained to GaN. This ability to grow thicker coherently-strained AlN interlayers by MBE is believed to come from the lower growth temperatures utilized by MBE. This gives additional motivation to further investigate MBE-grown N-polar GaN HEMT structures.

3.5 Conclusion:

In this chapter the fundamentals of Ga-rich PAMBE was summarized which should help the reader to better understand the experimental results presented in the following chapter. Published experimental and theoretical results reveal that dislocations arising from lattice mismatch can lead to coulombic scattering, current leakage and rough surface morphology in GaN – all of which can impede device performance. Devices grown on bulk GaN substrates may alleviate these effects by yielding films with an order of magnitude or lower TDD. Due to the non-periodic nature of alloys, random alloy scattering remains one of the chief causes of mobility degradation in GaN HEMTs. It has already been demonstrated that MBE has the potential to produce thicker coherently-strained AlN interlayers which could be used to better confine the 2DEG in the GaN channel thereby increasing mobility. Both dislocation-scattering and alloy-scattering can lead to power dissipation in HEMT amplifiers biased in class-A mode lowering device efficiency. The evidence brought forth in this chapter provides sufficient motivation for pursing growth of N-polar GaN on bulk GaN by MBE for high-performance and highly-efficient devices.

References:

[1] B. Romanczyk *et al.*, "Demonstration of Constant 8 W/mm Power Density at 10, 30, and 94 GHz in State-of-the-Art Millimeter-Wave N-Polar GaN MISHEMTs," *IEEE Trans. Electron Devices*, vol. 65, no. 1, pp. 45–50, Jan. 2018.

[2] S. Wienecke *et al.*, "N-Polar GaN Cap MISHEMT With Record Power Density Exceeding 6.5 W/mm at 94 GHz," *IEEE Electron Device Lett.*, vol. 38, no. 3, pp. 359–362, Mar. 2017.

[3] X. Zheng *et al.*, "Analysis of MOCVD SiNx Passivated N-Polar GaN MIS-HEMTs on Sapphire With High f_{max} $V_{DS,Q}$ *IEEE Electron Device Lett.*, vol. 39, no. 3, pp. 409–412, Mar. 2018.

[4] S. Rajan, A. Chini, M. H. Wong, J. S. Speck, and U. K. Mishra, "N-polar GaN/AlGaN/GaN high electron mobility transistors," *J. Appl. Phys.*, vol. 102, no. 4, p. 044501, Aug. 2007.

[5] M. H. Wong *et al.*, "N-polar GaN epitaxy and high electron mobility transistors," *Semicond. Sci. Technol.*, vol. 28, no. 7, p. 074009, Jul. 2013.

[6] M. A. Herman, M. A. Herman, and H. Sitter, *Epitaxy: physical principles and technical implementation*, Softcover reprint of the hardcover 1st edition 2004. Berlin Heidelberg: Springer, 2004.

[7] H. Umemoto, "A Clean Source of Ground-State N atoms: Decomposition of N_2 on Heated Tungsten," *Appl. Phys. Express*, vol. 3, no. 7, p. 076701, Jun. 2010.

[8] Irving. Langmuir and G. M. J. Mackay, "THE DISSOCIATION OF HYDROGEN INTO ATOMS. Part I. Experimental.," *J. Am. Chem. Soc.*, vol. 36, no. 8, pp. 1708–1722, Aug. 1914.

[9] A. Khandelwal, H. Niimi, G. Lucovsky, and H. H. Lamb, "Low-temperature Ar/N2 remote plasma nitridation of SiO2 thin films," *J Vac Sci Technol A*, vol. 20, no. 6, p. 9, 2002.

[10] E. C. H. Kyle, S. W. Kaun, P. G. Burke, F. Wu, Y.-R. Wu, and J. S. Speck, "High-electron-mobility GaN grown on free-standing GaN templates by ammonia-based molecular beam epitaxy," *J. Appl. Phys.*, vol. 115, no. 19, p. 193702, May 2014.

[11] N. Grandjean, M. Leroux, J. Massies, M. Mesrine, and M. Laügt, "Molecular Beam Epitaxy of GaN under N-rich Conditions using NH_3," *Jpn. J. Appl. Phys.*, vol. 38, no. Part 1, No. 2A, pp. 618–621, Feb. 1999.

[12] E. J. Tarsa, B. Heying, X. H. Wu, P. Fini, S. P. DenBaars, and J. S. Speck, "Homoepitaxial growth of GaN under Ga-stable and N-stable conditions by plasma-assisted molecular beam epitaxy," *J. Appl. Phys.*, vol. 82, no. 11, pp. 5472–5479, Dec. 1997.

[13] S. W. Kaun, M. H. Wong, U. K. Mishra, and J. S. Speck, "Molecular beam epitaxy for high-performance Ga-face GaN electron devices," *Semicond. Sci. Technol.*, vol. 28, no. 7, p. 074001, Jul. 2013.

[14] T. Zywietz, J. Neugebauer, and M. Scheffler, "Adatom diffusion at GaN (0001) and (000$\bar{1}$) surfaces," *Appl. Phys. Lett.*, vol. 73, no. 4, pp. 487–489, Jul. 1998.

[15] B. Heying, R. Averbeck, L. F. Chen, E. Haus, H. Riechert, and J. S. Speck, "Control of GaN surface morphologies using plasma-assisted molecular beam epitaxy," *J. Appl. Phys.*, vol. 88, no. 4, pp. 1855–1860, Aug. 2000.

[16] N. Takeuchi, A. Selloni, T. H. Myers, and A. Doolittle, “Adsorption and diffusion of Ga and N adatoms on GaN surfaces: Comparing the effects of Ga coverage and electronic excitation,” *Phys. Rev. B*, vol. 72, no. 11, Sep. 2005.
[17] J. Neugebauer, T. K. Zywietz, M. Scheffler, J. E. Northrup, H. Chen, and R. M. Feenstra, “Adatom Kinetics On and Below the Surface: The Existence of a New Diffusion Channel,” *Phys. Rev. Lett.*, vol. 90, no. 5, Feb. 2003.
[18] E. Monroy *et al.*, “Growth kinetics of N-face polarity GaN by plasma-assisted molecular-beam epitaxy,” *Appl. Phys. Lett.*, vol. 84, no. 18, pp. 3684–3686, May 2004.
[19] G. Koblmüller, J. Brown, R. Averbeck, H. Riechert, P. Pongratz, and J. S. Speck, “Ga Adlayer Governed Surface Defect Evolution of (0001)GaN Films Grown by Plasma-Assisted Molecular Beam Epitaxy,” *Jpn. J. Appl. Phys.*, vol. 44, no. No. 28, pp. L906–L908, Jul. 2005.
[20] F. A. Ponce, D. P. Bour, W. Götz, and P. J. Wright, “Spatial distribution of the luminescence in GaN thin films,” *Appl. Phys. Lett.*, vol. 68, no. 1, pp. 57–59, Jan. 1996.
[21] T. K. Zywietz, J. Neugebauer, and M. Scheffler, “The adsorption of oxygen at GaN surfaces,” *Appl. Phys. Lett.*, vol. 74, no. 12, pp. 1695–1697, Mar. 1999.
[22] M. Stutzmann *et al.*, “Playing with Polarity,” *Phys. Status Solidi B*, vol. 228, no. 2, pp. 505–512, Nov. 2001.
[23] S. Keller *et al.*, “Recent progress in metal-organic chemical vapor deposition of (000-1) N-polar group-III nitrides,” *Semicond. Sci. Technol.*, vol. 29, no. 11, p. 113001, Nov. 2014.
[24] S. Keller *et al.*, “Influence of the substrate misorientation on the properties of N-polar GaN films grown by metal organic chemical vapor deposition,” *J. Appl. Phys.*, vol. 102, no. 8, p. 083546, Oct. 2007.
[25] S. Keller *et al.*, “Influence of the surface misorientation on the properties of N-polar AlGaN/GaN and InGaN/GaN heterostructures,” p. 15.
[26] C. Chèze *et al.*, “Step-flow growth mode instability of N-polar GaN under N-excess,” *Appl. Phys. Lett.*, vol. 103, no. 7, p. 071601, Aug. 2013.
[27] H. Turski *et al.*, “Unusual step meandering due to Ehrlich-Schwoebel barrier in GaN epitaxy on the N-polar surface,” *Appl. Surf. Sci.*, Apr. 2019.
[28] D. C. Look and J. R. Sizelove, “Dislocation Scattering in GaN,” *Phys. Rev. Lett.*, vol. 82, no. 6, pp. 1237–1240, Feb. 1999.
[29] S. Dayeh, A. Tanaka, W. Choi, and R. Chen, “(Invited) Strain Engineered Crack-Free GaN on Si for Integrated Vertical High Power GaN Devices with Si CMOS,” *ECS Trans.*, vol. 75, no. 8, pp. 711–723, Sep. 2016.
[30] S. Y. Ren and J. D. Dow, “Lattice-matching SiC substrates with GaN,” p. 4.
[31] P. Waltereit *et al.*, “Influence of AlN nucleation layers on growth mode and strain relief of GaN grown on 6H–SiC(0001),” *Appl. Phys. Lett.*, vol. 74, no. 24, pp. 3660–3662, Jun. 1999.
[32] B. Heying, E. J. Tarsa, C. R. Elsass, P. Fini, S. P. DenBaars, and J. S. Speck, “Dislocation mediated surface morphology of GaN,” *J. Appl. Phys.*, vol. 85, no. 9, pp. 6470–6476, May 1999.
[33] S. D. Lester, F. A. Ponce, M. G. Craford, and D. A. Steigerwald, “High dislocation densities in high efficiency GaN-based light-emitting diodes,” *Appl. Phys. Lett.*, vol. 66, no. 10, pp. 1249–1251, Mar. 1995.

[34] C. Gupta, Y. Enatsu, G. Gupta, S. Keller, and U. K. Mishra, "High breakdown voltage p-n diodes on GaN on sapphire by MOCVD: High breakdown voltage p-n diodes," *Phys. Status Solidi A*, vol. 213, no. 4, pp. 878–882, Apr. 2016.
[35] N. G. Weimann, L. F. Eastman, D. Doppalapudi, H. M. Ng, and T. D. Moustakas, "Scattering of electrons at threading dislocations in GaN," *J. Appl. Phys.*, vol. 83, no. 7, pp. 3656–3659, Apr. 1998.
[36] B. S. Simpkins, E. T. Yu, P. Waltereit, and J. S. Speck, "Correlated scanning Kelvin probe and conductive atomic force microscopy studies of dislocations in gallium nitride," *J. Appl. Phys.*, vol. 94, no. 3, pp. 1448–1453, Aug. 2003.
[37] D. G. Zhao *et al.*, "Effects of edge dislocations and intentional Si doping on the electron mobility of n-type GaN films," *Appl. Phys. Lett.*, vol. 89, no. 11, p. 112106, Sep. 2006.
[38] B. Pödör, "Electron Mobility in Plastically Deformed Germanium," *Phys. Status Solidi B*, vol. 16, no. 2, pp. K167–K170, 1966.
[39] S. W. Kaun, M. H. Wong, U. K. Mishra, and J. S. Speck, "Correlation between threading dislocation density and sheet resistance of AlGaN/AlN/GaN heterostructures grown by plasma-assisted molecular beam epitaxy," *Appl. Phys. Lett.*, vol. 100, no. 26, p. 262102, Jun. 2012.
[40] D. F. Storm *et al.*, "Microwave performance and structural characterization of MBE-grown AlGaN/GaN HEMTs on low dislocation density GaN substrates," *J. Cryst. Growth*, vol. 305, no. 2, pp. 340–345, Jul. 2007.
[41] D. Jena and U. K. Mishra, "Quantum and classical scattering times due to charged dislocations in an impure electron gas," *Phys. Rev. B*, vol. 66, no. 24, Dec. 2002.
[42] E. Ahmadi, "Growth Optimization of III-N Electronic Devices by Plasma-Assisted Molecular Beam Epitaxy," p. 146.
[43] H. Sakaki, T. Noda, K. Hirakawa, M. Tanaka, and T. Matsusue, "Interface roughness scattering in GaAs/AlAs quantum wells," *Appl. Phys. Lett.*, vol. 51, no. 23, pp. 1934–1936, Dec. 1987.
[44] U. Singisetti, M. Hoi Wong, and U. K. Mishra, "Interface roughness scattering in ultra-thin N-polar GaN quantum well channels," *Appl. Phys. Lett.*, vol. 101, no. 1, p. 012101, Jul. 2012.
[45] S. Arulkumaran, T. Egawa, H. Ishikawa, and T. Jimbo, "Characterization of different-Al-content AlGaN/GaN heterostructures and high-electron-mobility transistors on sapphire," p. 8.
[46] S. Kolluri *et al.*, "Influence of AlN interlayer on the anisotropic electron mobility and the device characteristics of N-polar AlGaN/GaN metal-insulator-semiconductor-high electron mobility transistors grown on vicinal substrates," *J. Appl. Phys.*, vol. 108, no. 7, p. 074502, Oct. 2010.
[47] A. Adikimenakis *et al.*, "Effect of AlN interlayers in the structure of GaN-on-Si grown by plasma-assisted MBE," *J. Cryst. Growth*, vol. 311, no. 7, pp. 2010–2015, Mar. 2009.
[48] I. P. Smorchkova *et al.*, "Two-dimensional electron-gas AlN/GaN heterostructures with extremely thin AlN barriers," p. 3.
[49] H. Li, Thesis (2018)
[50] S. A. Campbell, *Epitaxy: Science and Engineering of Microelectronic Fabrication*, Hardcover 2nd edition 2001; Oxford University Press (2001)
[51] N. W. Ashcroft, N. D. Mermin, *Solid State Physics*, Hardcover1st edition: Cengage Learning (1976)

[52] S. Dasgupta, Thesis (2011)
[53] Unknown Source

Chapter 4: Optimizing film quality for N-polar GaN grown on free-standing GaN by PAMBE

4.1 Introduction:

In the previous chapters the motivation for homoepitaxially grown HEMT structures was discussed however little was mentioned regarding past work of N-polar GaN grown on bulk GaN. Although there exists an abundant supply of literature on N-polar HEMTs grown on foreign substrates[1]–[3], published work of N-polar GaN HEMT structures grown on FS GaN substrates is scarce. This is in part due to the low supply and high cost of GaN substrates. Another reason, however, is that N-polar GaN grown on non-miscut bulk GaN substrates has yet to be optimized. It has been shown that N-polar GaN grown on miscut FS GaN substrates have yielded smooth surfaces virtually free of pits [4], [5], however, substrate manufactures tend to charge significantly more money for vicinal substrates – a problem compounded by the fact that bulk GaN substrates are already expensive compared to SiC, sapphire and Si(111). The central theme of this chapter is how smooth pit-free N-polar GaN grown on non-miscut GaN substrates was achieved using MBE.

This chapter is laid out as such: in section 4.2 there will be a discussion regarding the general experimental procedure used across each study. A more in-depth explanation of each respective study will be given in sections 4.3-9. Section 4.3 will discuss early results of N-polar GaN grown on FS GaN which exhibited a high density of faceted pits. There will also be a discussion regarding the many theories as to what caused pits to generate and how other groups were able to suppress them. Section 4.4 will show the first evidence suggesting surface pits in N-polar GaN could be caused by impurities on the surface. In section 5 we will finally show how these pits were fully suppressed and smooth epi was achieved by initiating the growth with a thin layer of AlN fully strained to the GaN. To further understand

the nature of the AlN initiation layer (AIL) a series of experiments were carried out including a series of growths initiated with different AlN thicknesses and how thicker layers of AlGaN, grown at different compositions, effected the surface and film quality. Section 6 will involve a discussion on the effects of C-doping by CBr_4 and how it influences surface morphology and film quality in N-polar GaN grown by MBE; evidence shown in this study will further support the theory that surface pits are generated by impurities. In section 8, growth in the presence of In-flux was also carried out to see if any improvements in film quality and surface morphology resulted from using In as a surfactant along with Ga.

4.2 Experimental details:

All samples in this study were grown in a Varian Gen II MBE system with conventional Al, Si and Ga effusion cells. A Riber RF-plasma source was used to supply active nitrogen for growth. For our group-five source, ultrahigh-purity nitrogen (99.9995% purity) was used. Growth conditions consisted of flowing 3 sccm of N_2 through the plasma source which was set to 250 watts. Chamber pressure during growth was approximately 3×10^{-5} Torr. To maintain Ga-rich conditions the Ga-flux used for both the GaN and AlN growth was kept constant at 4.4×10^{-7} torr while Al-flux for AlN growth was 1.4×10^{-7} torr. All AlN layers were grown in the presence of a Ga-flux in order to maintain a Ga-adlayer during growth. Under these conditions the growth rate was measured to be approximately 60 A/min. Carbon doping of was done using carbon tetra-bromide (CBr_4). CBr_4 was introduced to the system via an automated control valve to throttle the vapor pressure from a solid-source CBr_4 bubbler to a foreline and into the system [6].

Except for the first sample in section 3 (see Fig. 4.4.1), every sample underwent an ultra-violet (UV) ozone clean followed by a one-minute dip in hydrofluoric (HF) acid. The UV-ozone treatment was carried out in a Jelight M-144AX reactor where the substrates were exposed to O_3 gas and UV-light for 15 minutes followed by a one-minute purge. The UV-ozone treatment and the HF dip were then repeated two more times before 500 nm of Ti was deposited on the back of the wafers using an electron-beam evaporator. Every sample which was loaded into the chamber underwent a 3-step solvent clean for four minutes each in acetone, methanol and isopropyl alcohol respectively. Samples were mounted to 3" Si substrates by In before being loaded into the chamber. Substrate temperature was monitored during growth by an optical pyrometer calibrated by the melting point of Al. The Ga-adlayer was monitored using reflection high energy electron diffraction (RHEED). Growths were interrupted approximately every ten minutes to desorb excess Ga on the surface preventing the formation of droplets.

The surface of every sample grown in this study was characterized using an Asylum MFP-3D atomic force microscope (AFM). X-ray diffraction (XRD) measurements were performed using a Panalytical MED PRO which utilized a 2.2 kW Philips ceramic sealed tube source using a 1.5404 Å Cu Kα radiation. Film thickness was measured by interference fringe spacing taken from $\omega - 2\theta$ scans. O, C and Si impurity concentration as a function of film depth was measured using a Cameca IMS 7f Auto SIMS (secondary ion mass spectrometry). High-resolution transmission electron microscopy (HRTEM) imaging was also carried out on two samples along with convergent-beam electron diffraction (CBED).

4.3 Initial results of N-polar GaN grown directly on the N-face GaN substrate:

Initial N-polar HEMTs grown on bulk GaN by MBE demonstrated by Pasayat et al. exhibited a number of faceted pits on the surface which was believed to be inhibiting device performance [7]. These pits, or holes, are not uncommon in epitaxially grown GaN. They have appeared in N-polar and Ga-polar films grown by both MBE and MOCVD [4], [8]. In the past it has been suggested that pits, or holes, on the surface of epitaxially grown GaN arise from different types of surface terminated dislocations. Theoretical work done by F.C. Frank in 1950 suggests that the strain energy associated with surface terminated dislocations lead to line tension into the material resulting in a craters or dimples [9]. The theory proposed by Frank was supported by the experimental work of Heying et al. in 1999 where the surface of Ga-polar MBE grown GaN grown under different III/V ratios was analyzed by atomic force microscopy (AFM) [8]. It was shown that GaN grown under approximately stoichiometric conditions (III/V ~ 1) exhibited pin-like holes on top of spiral hillox. It was believed these holes terminated two pinned steps which create a spiral associating them with mixed-type dislocations [8]. In the same work, for MOCVD grown GaN, holes were observed at the edge of two tangentially terminated steps [8]. These tangentially terminated step-pits seen in MOCVD Ga-polar GaN [8][10] are more similar to the larger faceted fits seen in our MBE grown N-polar GaN grown on FS GaN [7] and what was is observed in Fig. 4.4.1 below. It was concluded that these tangentially terminated step-pits were associated with mixed dislocations; generation of two pinned steps implies the presence of a mixed type dislocation where the Burgers vector is equal to the c-axis lattice parameter of GaN [8].

Although dislocations may be a contributor to surface pits and depressions, the amount of pits seen on the epitaxially grown surface in [7], and later in section 4.4 of this chapter, were over an order of magnitude higher than the TD density which was reported by the substrate manufacture. Since homoepitaxy, in theory, should not generate any further dislocations due to lattice mismatch, it is unlikely that dislocations were the only contributor to pits on the surface. In 2019 Turski at al. proposed a different theory in which holes on the surface were generated by unusual step-meandering; formation of pits can occur when one meander moves slower than another [11]. Unusual step-meandering is more likely to occur when epitaxial film is grown on a non-vicinal substrate as there are no periodic step-structure for which the film can grow on. Holes or pits may form in the slowly growing part of a step meander when two adjacent steps connect [11]. Theoretical work done by Krzyzewski et al. proposed step-flow growth could be achieved for N-polar GaN grown on FS GaN free of holes and depressions when a miscut substrate was used [5]. It was first shown by Cheze et al. that when growing N-polar GaN on non-miscut GaN by MBE, surface pits were eliminated by using a GaN substrate with a 17^{o} miscut grown under Ga-rich conditions [4]. Later it was shown that a using a substrate with only a 4^{o} miscut grown under slightly N-rich conditions yielded a smooth step-like surface free of holes and pits [11]. Using miscut foreign substrates is common practice in MOCVD to achieve smooth N-polar films [12], [13], however, there is little published work showing smooth, pit-free N-polar GaN grown on non-miscut bulk GaN substrates.

4.4 UV-ozone treatment:

Four samples in total were grown to study the effects of the UV-ozone clean. For samples A1-2, 200 nm of GaN was grown directly on the bulk GaN substrate. The first sample, labeled A1, was not subjected to any UV-ozone clean however both samples were subjected to the standard solvent clean discussed in the previous section before being loaded into the chamber. Sample A2 was subjected to the 3x UV-ozone clean and HF dip described in section 4.2. AFM micrographs showing the surfaces of samples A1-2 are displayed in figure 4.4.1 below. For samples AA1-2, 400 nm of GaN was grown directly on the bulk GaN substrate. Just like in A1-2, AA1 was not subjected to the UV-ozone treatment whereas AA2 was subjected to the UV-ozone clean. The AA-series samples were characterized by SIMS to see impurity concentration as a function of depth and the resulting SIMS data is displayed in figure 4.4.2 below.

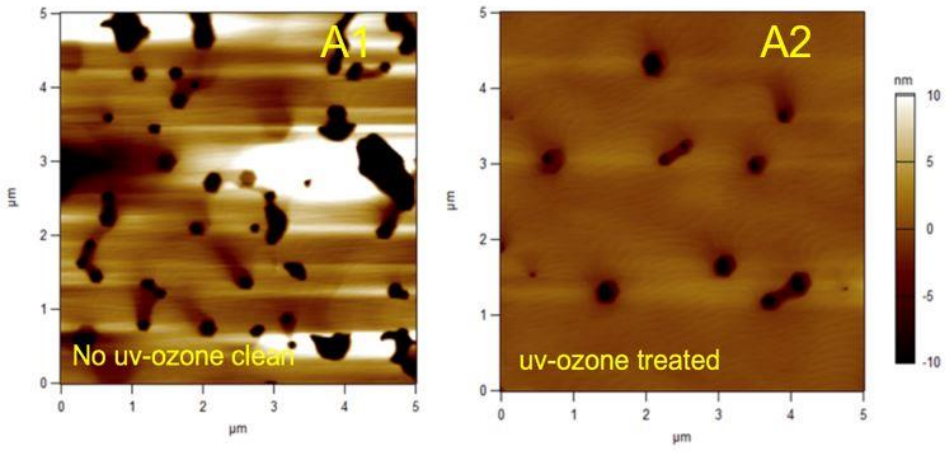

Figure 4.4.1: AFM micrograph for sample A1 which was only subjected to the standard solvent clean (left) and for sample A2 which was subjected to a 3x UV-ozone clean before growth (right)

From Fig. 4.4.1 above it is clear that there is a reduction in surface pits as a result of the UV-ozone clean, however, these pits are not removed completely. From figure 4.4.2 little change is seen for O and Si concentration at the regrowth interface for AA1 or AA2

however we do see an order of magnitude reduction in C-concentration for AA2 with respect to AA1 ($6 \times 10^{18} cm^{-3}$ to $6 \times 10^{17} cm^{-3}$ for AA1 and AA2 respectively).

It was thought that oxidizing the substrate surface by ultra-violet light and ozone gas followed by stripping said oxide via a hydrofluoric acid (HF) dip could rid the surface of such impurities. This UV-ozone treatment has been used successfully in the past to remove residual Si from Si-doped GaN for dielectric growth [14], [15]. It is clear from figure 4.4.2 that there is a buildup of impurities at the substrate/epi interface. In addition to residual impurities left over from polishing and processing done by the substrate manufacture, impurities may also accumulate on the surface when the wafer is exposed to atmosphere or from gettering inside the chamber [16]. It was believed that step-flow growth was hindered around regions with large clusters of impurities leading to the generation of pits. Comparing both figure 4.4.1 and 4.4.2 it can be concluded that the UV-ozone treatment suppresses some of the impurities, mainly carbon, but did not eliminate them completely. Therefor some other approach must be performed to mitigate the issue of surface-pits.

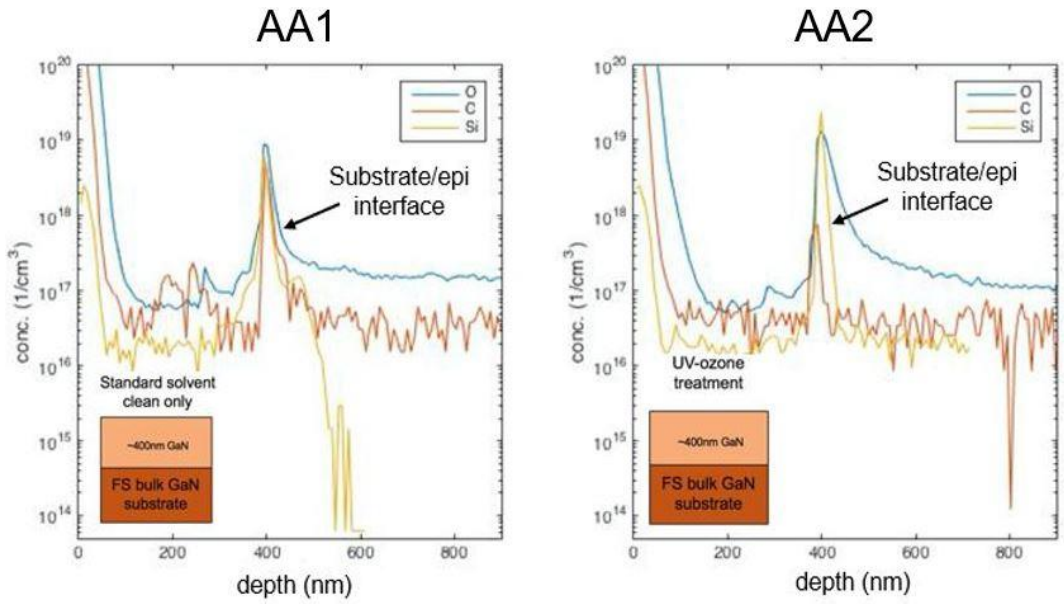

figure 4.4.2: SIMS results shown for 400 nm of GaN grown directly on a FS GaN substrate which was only subjected to a standard solvent clean only (left – AA1) and one which was subjected to the UV-ozone treatment as described in section 4.2 (right – AA2). From this figure we don't see much of a change in O and Si concentration at the regrowth interface however we do see a reduction in C-concentration.

4.5 Suppression of pits with the AlN initiation layer (AIL):

In the past thin layers of Al/group-five films have been used as nucleation layers and as barriers for impurities during epitaxial growth. A 20 nm AlAs layer, for example, had been used successfully by J. Ibbetson et al. as a diffusion barrier between doped and undoped GaAs [29]. Similarly, for GaN grown on SiC, thicker layers, about 70 nm, of AlN grown under nitrogen-rich conditions have also been used to block impurities from the SiC substrate from diffusing into the MBE-grown HEMT structures [16],[2],[17]. In addition to acting as a diffusion barrier between film layers, AlN has proven to be an effective nucleation layer for heteroepitaxial growth. In 2010 Li et al. demonstrated an improvement in surface

morphology by initiating the growth of 70% AlGaN with a few monolayers of AlN grown directly on a GaN buffer [18].

To see the effect of initiating growth with AlN three samples were grown which were labeled B1-3. B1 was initiated with 3 nm of GaN followed by 2 nm of AlN followed by 250 nm of GaN. B2 was initiated with 2 nm of AlN followed by 250nm of GaN. For B3, 250 nm of GaN was grown directly on the substrate. All samples underwent the UV-ozone treatment described in section 4.4. AFM images shown in figure 4.5.1 confirm that the 2 nm AIL leads to the elimination of pits on the surface for B1. The AFM micrograph of B1 suggests that pits are generated at the substrate/epi interface and not later during the growth and that the AlN cannot suppress the growth of pits once they have already been generated. The SIMS results and AFM micrographs shown in figure 4.4.1 and 4.4.2 support this theory, which is that pits are generated by impurities at the substrate/epi interface.

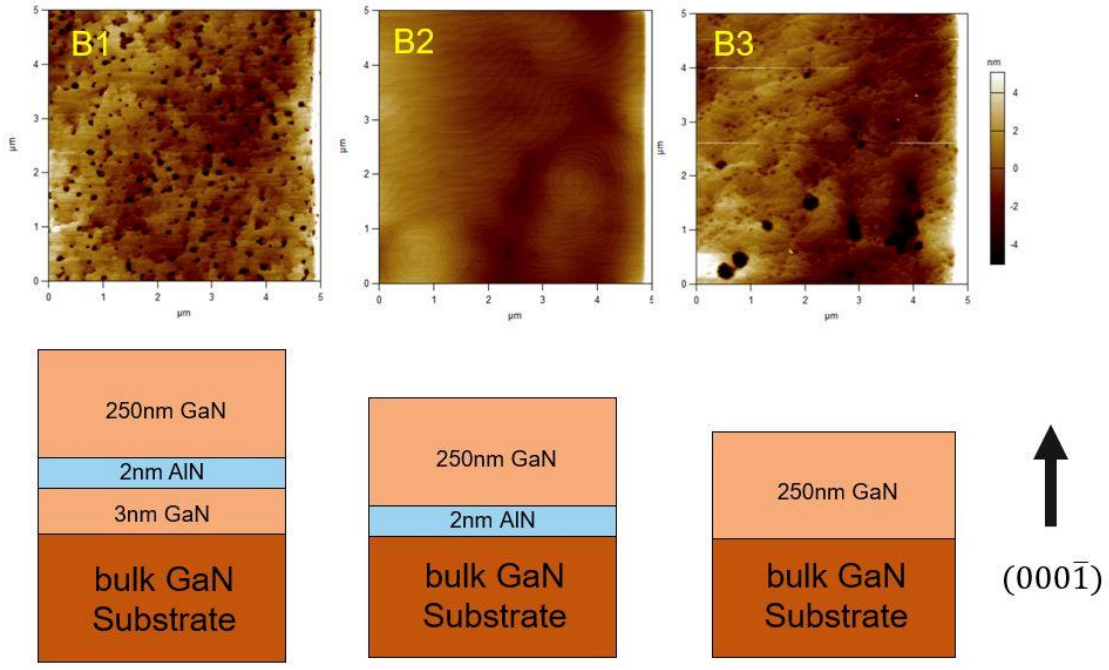

Figure 4.5.1: B-series AFM micrographs (top) with corresponding structures below.

TEM images shown in figure 4.5.2 suggest two possible sources of how pits are generated when growing on the substrate surface. The HRTEM image for B2 shown in figure 4.5.2a reveals that the AlN/substrate interface is rougher than the AlN/epi interface. Given Al's natural tendency to bond to other species with respect to Ga and N it is likely that the incoming Al-flux absorbs impurities on the surface. As the AlN continues to grow the surface becomes more even and smooth. It is on this abrupt, impurity free, AlN surface that smooth GaN can grow in step-flow mode without generating pits. Provided the AlN is thin enough such that it is fully strained to the GaN, no new dislocations will be generated due to lattice mismatch between AlN and GaN. Another possible theory as to how the pits are generated lies in the TEM image shown in 4.5.2b where we see a large number of defects in the substrate. Pits maybe generated where these defects intersect with the surface. Given that AlN buffers have shown to produce smooth GaN when grown on non-native substrates [2], [16], [17],[19] it is likely that AlN is less sensitive to generating pits around defects compared to GaN. Of course, it is also possible that pits may have been generated by both defects and impurities. It is known that the N-polar surface is particularly sensitive to absorbing impurities such as oxygen [20]. To make a more accurate conclusion as to why pits are generated at the interface and how the AIL suppresses the pits is subject to further investigation and outside the scope of this paper. However, it can be concluded that the AIL serves as a nucleation layer for homoepitaxial growth of GaN on non-miscut GaN.

This dramatic improvement in surface morphology resulting from the AIL begs the question as to whether the initial AlN layer inverted the polarity of the GaN film. That is, did the film grown following the AIL become Ga-polar? It has been demonstrated that N-polar AlN buffer layers used to grow GaN by PAMBE on (111) Si under highly metal-rich

conditions inverted the polarity of the AlN [19]. CBED patterns shown in figure 4.5.2b for the substrate and the epi grown film for this study, compared with simulated results, reveal that no polarity inversion took place due to the AIL and both the substrate and the epi are indeed N-polar. Another method showing how to verify surface polarity of GaN using potassium hydroxide (KOH) is given in appendix A.3

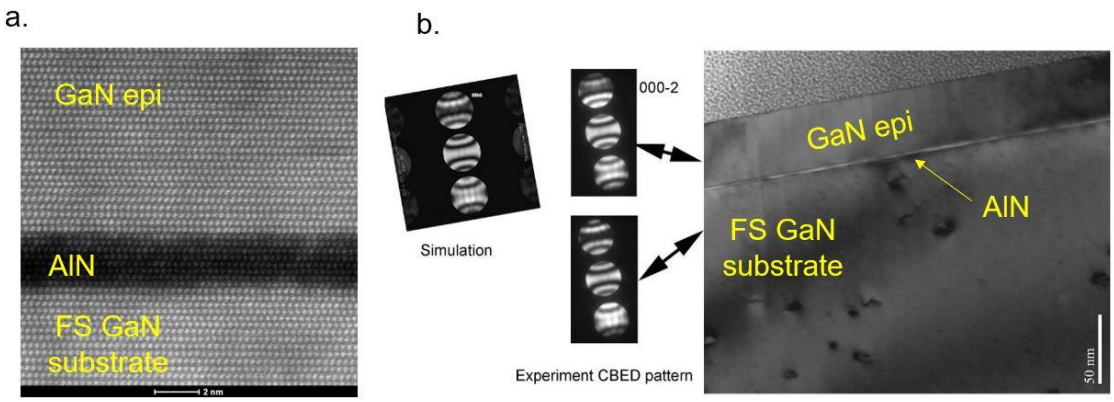

Figure 4.5.2: a. Left – HRTEM image taken for B2 at the AIL, b. Right-TEM images and CBED patterns for B2 showing both the simulated and experimental patterns for above and below the AIL.

4.6 Different compositions of AlGaN grown directly on the bulk GaN substrate:

To obtain further insight into the improvements in surface morphology as a result of the AIL it seemed interesting to see what would happen if different compositions of AlGaN were deposited directly on the surface of the N-face substrate. For samples C1-4 30 nm of AlGaN was grown directly on the N-face substrate with Al-compositions of 6, 17, 30 and 81% respectively. The resulting XRD $\omega - 2\theta$ scans and AFM micrographs are depicted in figure 4.6.1 below.

Observing the AFM micrographs in figure 4.6.1 we see the formation of what appear to be spiral hillox spread across the surface in C1. These spiral hillox increase dramatically and become more pronounced in sample C2 when we increase Al-composition from 6% to 17%. The surface density of these spiral hillox drop as we go to C3 where 30% Al-composition is used and they almost completely disappear when we go to the 81% Al-composition in C4. The lines running across the surface in C4 arise from cracking of the films due to stress from in-plane lattice mismatch between GaN and $Al_{0.81}Ga_{0.19}N$. Given that these hillox disappear as we go to higher Al-compositions, corresponding to a higher lattice mismatch, it can be assumed that they are not entirely related to dislocations.

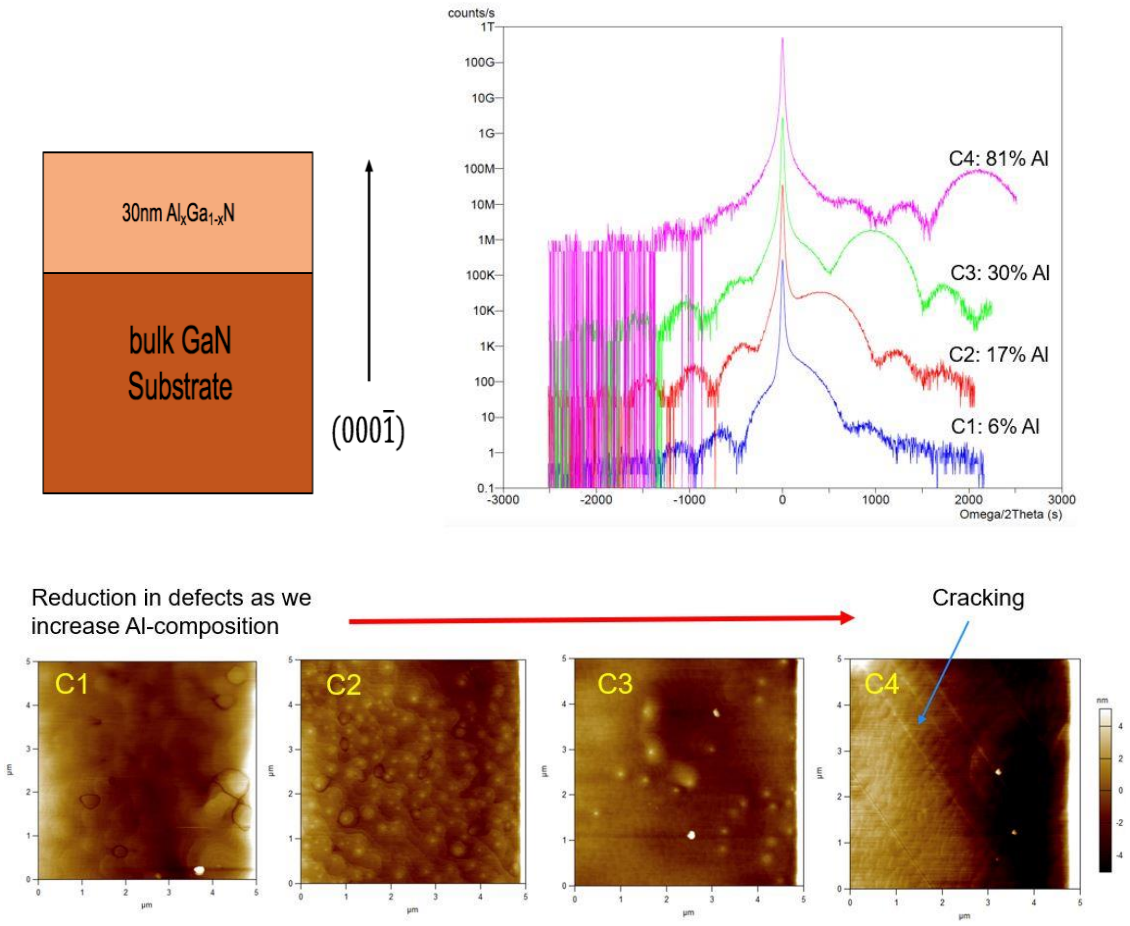

Figure 4.6.1. Top (left): illustration of grown structure for C1-4, Top (right): XRD $\omega - 2\theta$ scan results for samples C1-4. Bottom: AFM micrographs for samples C1-4 where 30 nm of AlGaN was grown directly on bulk GaN substrates with an Al-composition of 6, 17, 30 and 81% respectively.

4.7 Thicker AIL Layers:

Based off the dramatic results obtained by using the 2 nm AIL it seemed necessary to investigate if thicker AILs would further improve film quality and surface morphology. Samples C1-C4 were each initiated with a 2 nm, 4 nm, 6 nm and 8 nm AIL respectively. The resulting AFM images and XRD rocking curve data is shown in figure 4.7.1 below. AFM micrographs in figure 4.7.1a shows that for the 2 nm and 4 nm AIL the step-meandering is more random and more defects appear on the surface whereas in the case of the 6 nm and 8

nm AIL the surface is ultra-smooth and the steps are far more periodic. While the AFM micrograph for C3 (6 nm AIL) has almost no step-meandering, similar to what would be seen in a miscut substrate, C4 does has step-meandering, however, the distance between meanders is more uniform and the terrace lengths are much shorter. Rocking curve results in figure 4.7.1b suggests an increase in film quality as we go to thicker AILs. The reciprocal space map (RSM) scan for sample C4 shown in figure 4.7.2 reveals that the 8 nm AIL is coherently strained to the GaN.

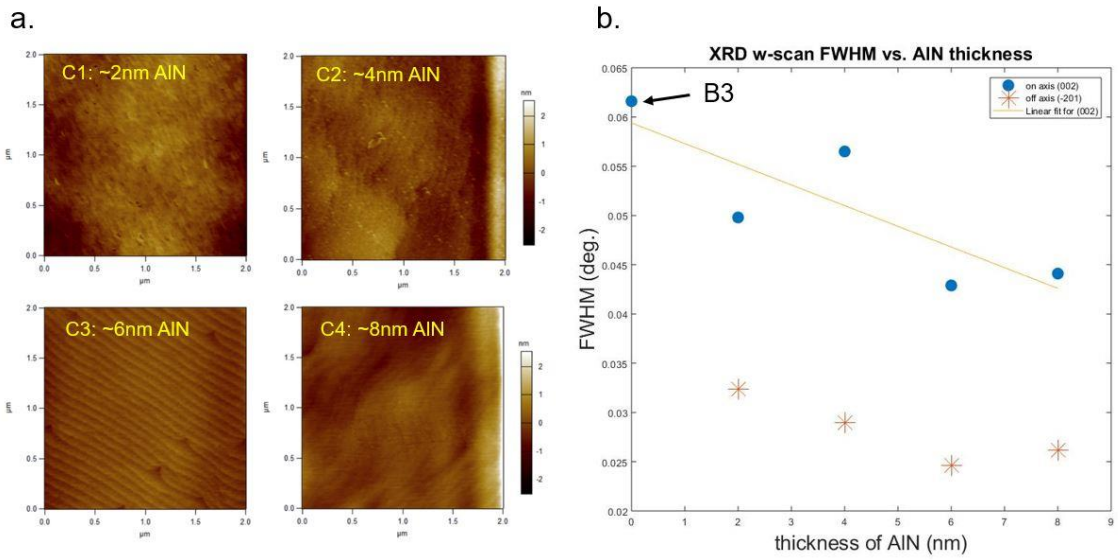

Figure 4.7.1: a. (left) AFM micrographs for C-series samples, b. (right) XRD w-scan FWHM values for all of the C-series samples as well as B4 and B3. Because samples B3 was only 5mm by 5mm it was not possible to perform off-axis scans because the magnetic holders used to mount the sample blocked it from the source radiation.

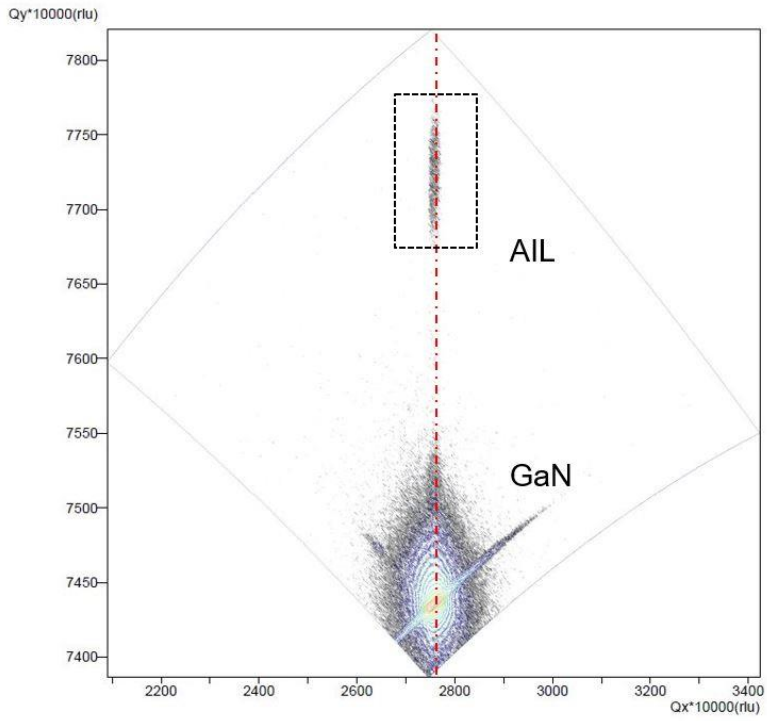

Figure 4.7.2: XRD RSM scan done at the (105) plane for the sample C4 showing the 8 nm AlN initiation layer (AIL) is fully strained to the GaN

The improvement in surface morphology and film quality, as seen in figure 4.7.1 indicates that utilizing thicker AILs leads to higher quality films for the GaN grown after the AIL. As mentioned before from TEM images in Fig. 4.5.2, tt is believed that as the AIL grows thicker and thicker it absorbs more impurities and the surface becomes more smooth thereby making the subsequence GaN more smooth. Another interesting observation is that the 8 nm AIL remains coherently strained to the GaN. It has been reported by Smorchkova at al. that MBE-grown AlN interlayers grown in Ga-polar GaN films have been shown to relax and crack for AlN thicknesses less that 4.7 nm [21]. However, in 2017 Li reported that 8.1 nm AlN interlayers grown in N-polar GaN by MOCVD were coherently strained to GaN [30]. Even thicker coherently strained AlN interlayers, verified by XRD-RSMs and TEM

imaging, have been reported in GaN grown by PAMBE [22]. This is particulary interesting since the following chapter will present device structures with thick graded AlGaN back-barriers and pure AlN back-barriers which we hope to grow my MBE.

4.8 C-doping in GaN:

Carbon doping by CBr_4 in MBE-grown GaN has been used extensively to grow semi-insulating GaN buffer layers for HEMTs [23]. It has been demonstrated that when C-atoms occupy N-sites of the naturally N-type GaN they act as deep level acceptors pulling the Fermi-level away from the conduction band thus making the film more insulating [6], [24]. This enables the fabrication of semi-insulating GaN for transistor applications. Because of this it was necessary to see how C-doping effected the surface morphology for N-polar GaN grown on bulk GaN.

For samples D1-D3 growth was initiated with 2 nm of AlN followed by 200 nm of GaN:C with CBr_4 foreline pressure of 20, 40 and 60 mTorr which corresponded to a C-doping concentration of approximately $5.3 \times 10^{19}, 2.5 \times 10^{20}\ and\ 8.3 \times 10^{20}\ cm^{-3}$ respectively. C-concentration as a function of CBr_4 foreline pressure was determined from a multi-layered C-doped SIMS stack carried out in a previous experiment (see appendix A.5). AFM micrographs showing the surface morphology of D1-3 are depicted in figure 4.8.1 below.

The AFM micrographs in figure 4.8.1 reveal that the surface pits return for high C-concentrations. Sample D1, where C-doping was $5.3 \times 10^{19}\ cm^{-3}$, exhibited almost no pits however it can be seen that in certain regions, particularly where two adjacent step meanders meet, there exists depressions which could potentially lead to the formation of pits had the

film continued to grow. From figure 4.8.1 we see that these pits return for some C-doping concentration between $5.3 \times 10^{19} - 2.5 \times 10^{20}\ cm^{-3}$. The results of this study suggest that surface pits on N-polar GaN films can be generated by several factors including surface defects, impurities, dislocations and slow-moving step meanders, and that the AIL decouples the substrate surface from the epitaxially grown GaN.

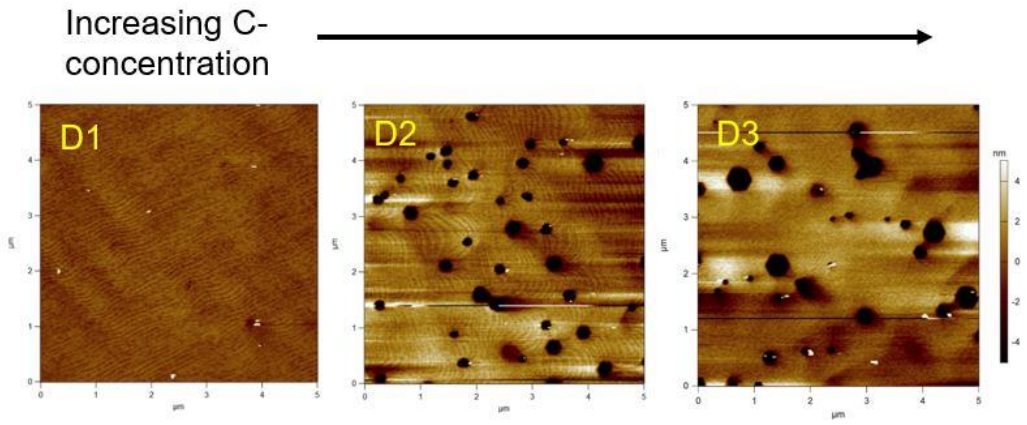

Figure 4.8.1: AFM micrographs for samples D1-D3 (left to right respectively) where C-doping is varied from $5.3 \times 10^{19}, 2.5 \times 10^{20}\ and\ 8.3 \times 10^{20}\ cm^{-3}$ respectively.

4.9 Using In as a surfactant:

Theoretical work done by Neugenbauer et al. showed that the adatom diffusion barrier for N under an In-adlayer is 0.5 eV whereas the diffusion barrier on the bare surface is 1.3 eV [25]. This begs the question as to whether or not using an In-adlayer during growth would produce smoother films than a Ga-adlayer. Using In as a surfactant has been used extensively for Ga-polar films and N-polar films by MOCVD [26], [27] and by MBE of Ga-polar films [28] with some success. To use In as a surfactant, however, growth conditions must be used such that almost no In is incorporated when growing GaN. Fortunately, at the growth temperatures used in this study (~730^{o} C) the sticking coefficient for In should be

approximately zero [28]. Therefor it is unlikely any In-incorporation will occur if growths are done in the presence of In-flux.

Four samples were used, labeled E1-4, to see the effects of subjecting the samples to an In-flux during growth. Samples E1-2 were each grown in the presence of an In-flux of $2 \times 10^{-7}\ torr$ at 680° and 740° respectively. Samples E3-4 were each grown with no In-flux at 680° and 740° respectively. Ga-flux was kept constant at approximately $4 \times 10^{-7}\ torr$ for all samples in this study. It should be noted that in this study that the adlayer is not purley In but rather a mixture of In and Ga. Table 4.9.1 shows the growth conditions and resulting rocking-curve data for the In-flux experiment. AFM micrographs and XRD w-scan FWHM plot is shown in figure 4.9.1 below.

Table 4.9.1: growth temperature, In-flux, on-axis and on-axis w-scan measurements for E-series experiment in which In was used a surfactant

Sample	Growth Temp	F_{In}	FWHM (002)	FWHM (201)
name	(Deg. C)	(Torr)	(deg.)	(deg.)
E1	680	2e-7	0.048	0.033
E2	740	2e-7	0.083	0.042
E3	680	-	0.036	0.03
E4	740	-	0.052	0.026

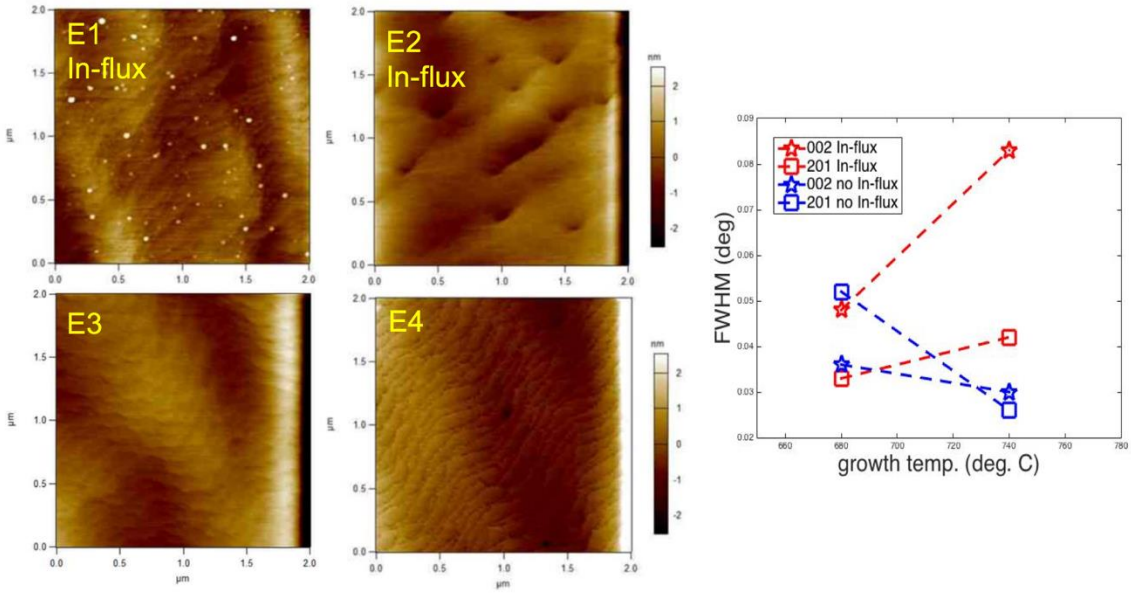

Figure 4.9.1: AFM micrographs (left) and on and off-axis w-scan FWHM measurements (right) given for the samples shown in table 4.9.1.

In terms of surface morphology, it appears that the films which were subjected to the In-flux during growth exhibited worse surface morphology as indicated by the more random step meandering see in the AFM micrographs in Fig. 4.9.1 for E1-2 when compared to the surfaces of E3-4 which exhibit rather uniform step patterns. Furthermore, sample E2 has a number of surface depressions whereas E1 exhibited what appeared to be metal droplets on the surface. XRD rocking curve results shown in Fig. 4.8.1 and table 4.8.1 display no difference in terms of films quality for any of the samples grown at 680^{o} however there is a clear increase of the FWHM for both samples grown in the presence of In-flux (E1-2) when compared to the samples grown under normal conditions (E2-3) at 740^{o}. This decrease in film quality and surface morphology for the samples subjected to In-flux could be attributed to impurities in the In-cell, however, it is clear from this experiment that growing in the

presence of In-flux does not yield any improvement over films grown under normal purely Ga-rich conditions.

4.10 Conclusion:

The major obstacle in growing N-polar films on free-standing bulk GaN substrates is producing pit-free films with smooth surface morphology. This problem is rooted in the N-polar surface which is particularly sensitive in absorbing impurities [20]. It can be concluded from the studies shown in this chapter that these surface impurities play a major role in the generation of faceted pits on the film surface. It was found that by subjecting the substrates to a 3x UV-ozone clean and initiating growth with a thin layer of AlN, dubbed the AIL, grown under Ga-rich conditions created an ultra-smooth surface by absorbing these surface impurities thus decoupling the MBE grown GaN from the substrate. Thicker AILs, up to 8 nm, proved to further improve surface morphology and films quality while remaining coherently strained to GaN. It was observed that these surface-pits returned for C-doping concentrations above $5.3 \times 10^{19}\ cm^{-3}$ further suggesting that pits were caused by impurities. Growing in the presence of In-flux had an adverse effect on surface morphology and film quality. Further experiments could be carried out to understand the true mechanism of the AIL and at what critical thickness the AlN relaxes. This work, however, demonstrates that smooth pit-free N-polar GaN can be grown by PAMBE on bulk GaN which could thus be used to grow high-quality N-polar HEMT structures.

References:

[1] E. Ahmadi *et al.*, "N-face GaN/AlN/GaN/InAlN and GaN/AlN/AlGaN/GaN/InAlN high-electron-mobility transistor structures grown by plasma-assisted molecular beam epitaxy on vicinal substrates," *Semicond. Sci. Technol.*, vol. 30, no. 5, p. 055012, May 2015.

[2] S. Rajan, M. Wong, Y. Fu, F. Wu, J. S. Speck, and U. K. Mishra, "Growth and Electrical Characterization of N-face AlGaN/GaN Heterostructures," *Jpn. J. Appl. Phys.*, vol. 44, no. No. 49, pp. L1478–L1480, Nov. 2005.

[3] M. H. Wong, Y. Pei, J. S. Speck, and U. K. Mishra, "High power N-face GaN high electron mobility transistors grown by molecular beam epitaxy with optimization of AlN nucleation," *Appl. Phys. Lett.*, vol. 94, no. 18, p. 182103, May 2009.

[4] C. Chèze *et al.*, "Step-flow growth mode instability of N-polar GaN under N-excess," *Appl. Phys. Lett.*, vol. 103, no. 7, p. 071601, Aug. 2013.

[5] F. Krzyżewski, M. A. Załuska-Kotur, H. Turski, M. Sawicka, and C. Skierbiszewski, "Miscut dependent surface evolution in the process of N-polar GaN(000$\bar{1}$) growth under N-rich condition," *J. Cryst. Growth*, vol. 457, pp. 38–45, Jan. 2017.

[6] D. S. Green, U. K. Mishra, and J. S. Speck, "Carbon doping of GaN with CBr4 in radio-frequency plasma-assisted molecular beam epitaxy," *J. Appl. Phys.*, vol. 95, no. 12, pp. 8456–8462, Jun. 2004.

[7] S. S. Pasayat *et al.*, "First demonstration of RF N-polar GaN MIS-HEMTs grown on bulk GaN using PAMBE," *Semicond. Sci. Technol.*, vol. 34, no. 4, p. 045009, Apr. 2019.

[8] B. Heying, E. J. Tarsa, C. R. Elsass, P. Fini, S. P. DenBaars, and J. S. Speck, "Dislocation mediated surface morphology of GaN," *J. Appl. Phys.*, vol. 85, no. 9, pp. 6470–6476, May 1999.

[9] F. C. Frank, "Capillary equilibria of dislocated crystals," *Acta Crystallogr.*, vol. 4, no. 6, pp. 497–501, Nov. 1951.

[10] E. J. Tarsa, B. Heying, X. H. Wu, P. Fini, S. P. DenBaars, and J. S. Speck, "Homoepitaxial growth of GaN under Ga-stable and N-stable conditions by plasma-assisted molecular beam epitaxy," *J. Appl. Phys.*, vol. 82, no. 11, pp. 5472–5479, Dec. 1997.

[11] H. Turski *et al.*, "Unusual step meandering due to Ehrlich-Schwoebel barrier in GaN epitaxy on the N-polar surface," *Appl. Surf. Sci.*, Apr. 2019.

[12] S. Keller *et al.*, "Influence of the surface misorientation on the properties of N-polar AlGaN/GaN and InGaN/GaN heterostructures," p. 15.

[13] S. Keller *et al.*, "Recent progress in metal-organic chemical vapor deposition of (000-1) N-polar group-III nitrides," *Semicond. Sci. Technol.*, vol. 29, no. 11, p. 113001, Nov. 2014.

[14] C. Gupta *et al.*, "Comparing electrical performance of GaN trench-gate MOSFETs with *a* -plane and m-plane sidewall channels," *Appl. Phys. Express*, vol. 9, no. 12, p. 121001, Dec. 2016.

[15] C. Gupta *et al.*, "In Situ Oxide, GaN Interlayer-Based Vertical Trench MOSFET (OG-FET) on Bulk GaN substrates," *IEEE Electron Device Lett.*, vol. 38, no. 3, pp. 353–355, Mar. 2017.

[16] S. W. Kaun, M. H. Wong, U. K. Mishra, and J. S. Speck, "Molecular beam epitaxy for high-performance Ga-face GaN electron devices," *Semicond. Sci. Technol.*, vol. 28, no. 7, p. 074001, Jul. 2013.
[17] S. W. Kaun, M. H. Wong, U. K. Mishra, and J. S. Speck, "Correlation between threading dislocation density and sheet resistance of AlGaN/AlN/GaN heterostructures grown by plasma-assisted molecular beam epitaxy," *Appl. Phys. Lett.*, vol. 100, no. 26, p. 262102, Jun. 2012.
[18] G. Li, Y. Cao, H. G. Xing, and D. Jena, "High mobility two-dimensional electron gases in nitride heterostructures with high Al composition AlGaN alloy barriers," *Appl. Phys. Lett.*, vol. 97, no. 22, p. 222110, Nov. 2010.
[19] M. Agrawal, K. Radhakrishnan, N. Dharmarasu, and S. S. Pramana, "Effect of III/V ratio on the polarity of AlN and GaN layers grown in the metal rich growth regime on Si(111) by plasma assisted molecular beam epitaxy," *Jpn. J. Appl. Phys.*, vol. 54, no. 6, p. 065701, Jun. 2015.
[20] T. K. Zywietz, J. Neugebauer, and M. Scheffler, "The adsorption of oxygen at GaN surfaces," *Appl. Phys. Lett.*, vol. 74, no. 12, pp. 1695–1697, Mar. 1999.
[21] I. P. Smorchkova *et al.*, "Two-dimensional electron-gas AlNÕGaN heterostructures with extremely thin AlN barriers," p. 3.
[22] A. Adikimenakis *et al.*, "Effect of AlN interlayers in the structure of GaN-on-Si grown by plasma-assisted MBE," *J. Cryst. Growth*, vol. 311, no. 7, pp. 2010–2015, Mar. 2009.
[23] C. Poblenz, P. Waltereit, S. Rajan, S. Heikman, U. K. Mishra, and J. S. Speck, "Effect of carbon doping on buffer leakage in AlGaN/GaN high electron mobility transistors," *J. Vac. Sci. Technol. B Microelectron. Nanometer Struct.*, vol. 22, no. 3, p. 1145, 2004.
[24] J. L. Lyons, A. Janotti, and C. G. Van de Walle, "Carbon impurities and the yellow luminescence in GaN," *Appl. Phys. Lett.*, vol. 97, no. 15, p. 152108, Oct. 2010.
[25] J. Neugebauer, T. K. Zywietz, M. Scheffler, J. E. Northrup, H. Chen, and R. M. Feenstra, "Adatom Kinetics On and Below the Surface: The Existence of a New Diffusion Channel," *Phys. Rev. Lett.*, vol. 90, no. 5, Feb. 2003.
[26] S. Keller, S. Heikman, I. Ben-Yaacov, L. Shen, S. P. DenBaars, and U. K. Mishra, "Indium-surfactant-assisted growth of high-mobility AlN/GaN multilayer structures by metalorganic chemical vapor deposition," *Appl. Phys. Lett.*, vol. 79, no. 21, pp. 3449–3451, Nov. 2001.
[27] D. Won, X. Weng, and J. M. Redwing, "Metalorganic chemical vapor deposition of N-polar GaN films on vicinal SiC substrates using indium surfactants," *Appl. Phys. Lett.*, vol. 100, no. 2, p. 021913, Jan. 2012.
[28] F. Widmann, B. Daudin, G. Feuillet, N. Pelekanos, and J. L. Rouvière, "Improved quality GaN grown by molecular beam epitaxy using In as a surfactant," *Appl. Phys. Lett.*, vol. 73, no. 18, pp. 2642–2644, Nov. 1998.
[29] J. Ibbetson, Thesis (2007)
[30] H. Li, Thesis (2018)

Chapter 5: N-polar HEMT structures with thick AlN back-barriers

5.1 Introduction:

Given that MBE-grown AlN-interlayers coherently strained to GaN can be grown thicker than what has been traditionally reported by MOCVD [1], [2], the investigation of N-polar HEMT structures which utilize ultra-thick AlN-interlayers or use a back-barrier consisting of pure AlN becomes of interest. Looking at the history of early MBE N-polar HEMT technology discussed in chapter one, Wong et al. demonstrated multiple devices which used a 2 nm AlN back-barrier, a dual 2 nm AlN back-barrier and a digital AlGaN back-barrier consisting only of GaN and AlN, all of which demonstrated adequate W-band device performance [3]–[5]. All of these devices, however, were grown on foreign substrates with a TDD on the order of 10^{10} cm^{-2}. In this section we present device structures similar to the MBE grown AlN-based back-barrier devices which were utilized in the past [3]–[5], however, these devices are intended to be grown on bulk-GaN substrates and MOCVD grown GaN-on-sapphire templates with TDDs of $10^{6} – 10^{8}$ cm^{-2} for comparisons. Ultimately, whether these device structures can be grown will depend on the amount of strain the GaN can sustain without relaxation or cracking in the presence of thick coherently-strained AlN layers.

In the preceding chapter it was shown that high-quality N-polar GaN grown on bulk GaN by PAMBE could be achieved by initiating growth with a thin layer of AlN grown under metal-rich conditions. With these growth conditions it is now possible to grow HEMT structures on bulk GaN by PAMBE with an order of magnitude or lower TDD than what has currently been reported. Furthermore, using PAMBE, thicker AlN interlayers can be grown which could hopefully lead to higher 2DEG mobility in the channel. In this chapter several

HEMT structures using pure AlN back-barriers (BBs) will be presented. However, thick AlN layers lead to strained heterointerfaces with higher piezoelectric charge which will produce significantly higher band-bending. This band bending will lead to a negatively polarized interface (NPI) behind the backbarrier with extremely high charge. To mitigate the NPI a highly-doped graded AlGaN barrier will need to be employed. Too high of doping behind the backbarrier and in the graded AlGaN layer could increase the effect of remote-ionized impurity scattering – something which was found to be negligible in previous N-polar HEMT structures which were doped no higher than $5 \times 10^{18}\ cm^{-3}$ [6]. Using simulations, however, some basic device structures can be realized for future work.

5.2 Proposed N-polar HEMT structures

Nine HEMT structures in total were simulated using the 1D Poisson solver Bandeng [9]. Each sample used a Si-doped graded AlGaN layer where Al composition was graded from 0-100%. Series A used an AlN backbarrier thickness of 2 nm with an AlGaN grade thickness of 10, 20 and 30 nm for A1-3 respectively. Series B used an AlN backbarrier thickness of 4 nm with an AlGaN grade thickness of 10, 20 and 30 nm for A1-3 respectively. Series C used an AlN backbarrier thickness of 6 nm with an AlGaN grade thickness of 10, 20 and 30 nm for A1-3 respectively. Si doping for the 10 nm GaN layer and graded AlGaN layer was chosen such that the Fermi-level was sufficiently above the valence band with minimal doping. Table 5.2.1 gives the details of each simulated device for A-C series. The corresponding band diagram, charge profile and 2DEG sheet charge as a function of AlGaN grade thickness is displayed in Fig. 5.2.1 below.

Table 5.2.1: AlN backbarrier HEMT series data based off simulations done on the 1D Poisson solver Bandeng [9]

	AlN thickness	**Grade thickness**	**Si doping**	**n_s**
name	(nm)	(nm)	(cm^{-3})	(cm^{-3})
A1	2	10	1.50E+19	7.70E+13
A2	2	20	1.20E+19	1.40E+14
A3	**2**	**30**	**9.00E+18**	**4.20E+13**
B1	4	10	1.50E+19	2.10E+14
B2	4	20	1.20E+19	3.20E+14
B3	4	30	9.00E+18	3.68E+14
C1	6	10	1.50E+19	4.50E+13
C2	6	20	1.20E+19	4.51E+13
C3	**6**	**30**	**9.00E+18**	**4.15E+13**

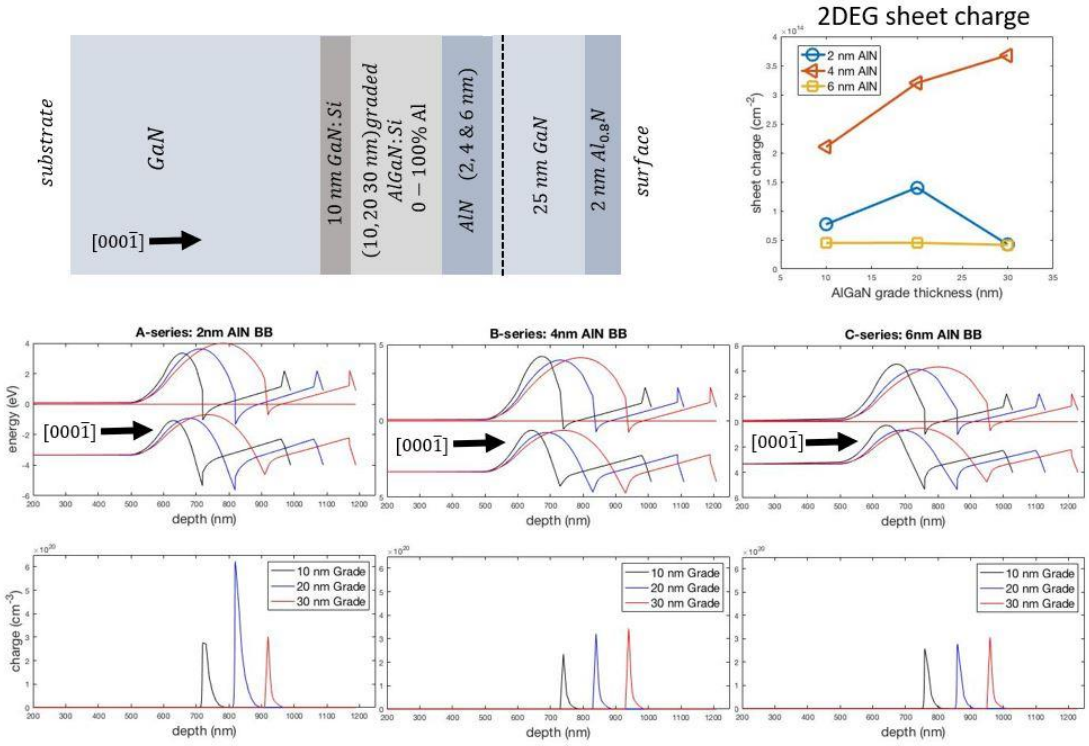

Figure 5.2.1: (bottom, left to right) band-diagrams (above) and charge profiles (below) for A-C series respectively. (Top - right) 2DEG sheet charge density as a function of AlGaN grade thickness. (Top-left) illustration of device structure.

Looking at the sheet charge vs. grade thickness plot in the top right corner of Fig. 5.2.1 we see that the structures with the 4 nm AlN BB (orange triangles) yielded the highest 2DEG sheet charges which further increases as a function of grade thickness. The structures with the 2 nm and 6 nm AlN BBs (blue circles) seem to show no real trend in terms of 2DEG sheet charge and grade thickness except that the 2DEG sheet charge, in both cases, peaks at an AlGaN grade thickness of 20 nm. The structures with the 2 nm AlN have a slightly higher 2DEG density when compared with the 6 nm AlN back-barrier samples (yellow squares).

The two structures in blue-bold writing shown in table 5.2.1 are the only two devices which are deemed practical for our purposes. For the B-series and A2 structures the 2DEG charge is too high for a HEMT channel. Khurgin et al. had demonstrated experimentally that saturation velocity in a 2DEG channel decays exponentially as a function of 2DEG sheet charge density - an effect which was attributed longitudinal optical (LO) phonon scattering by hot electrons in the GaN channel [7]. Structure A1, C1 and C2 all required Si-doping above 1e19 cm^{-3} to suppress the NPI; two high Si-doping could generate pits during growth as was demonstrated with the C-doping study in section 4.7. Too high Si-doping could also lead to significant remote-ionized impurity scattering in the channel.

5.3 Conclusion:

From the simulations carried out in this study two possible HEMT structures were realized which would be grown by PAMBE. In one case, structure A3 would consist of a 10 nm Si doped GaN layer behind a 30 nm Si-doped (9e18 cm^{-3}) graded AlGaN layer followed by a 2 nm undoped AlN back-barrier. The second structure, C3 would consist of a 10 nm Si doped GaN layer behind a 30 nm Si-doped (9e18 cm^{-3}) graded AlGaN layer followed by a 6

nm undoped AlN back-barrier. Sample C3 would be the most ideal because the 6 nm AlN back-barrier would create the greatest separation between the 2DEG and the Si-doped graded AlGaN thus lowering remote-ionized impurity scattering, however, this would depend on whether or not the 6 nm AlN backbarrier plus the 30 nm graded AlGaN layer would remain strained to the GaN. In reality a series of samples would have be grown with variations in Si-doping, AlN backbarrier thickness and graded AlGaN layer thickness to find a structure with optimum mobility and charge. Aside from the structures presented in this chapter one could also grow a similar structure to that shown in Fig. 2.3.3 used in [8] (30% AlGaN backbarrier) but with a thicker AlN interlayer to reduce alloy scattering. Mirrored devices could be grown on MOCVD grown GaN-on-sapphire and GaN-on-SiC substrates and compared with devices grown on bulk GaN. From the simulations in this chapter plus the growth recipes developed in chapter 5.

References:

[1] A. Adikimenakis *et al.*, "Effect of AlN interlayers in the structure of GaN-on-Si grown by plasma-assisted MBE," *J. Cryst. Growth*, vol. 311, no. 7, pp. 2010–2015, Mar. 2009.

[2] I. P. Smorchkova *et al.*, "Two-dimensional electron-gas AlNÕGaN heterostructures with extremely thin AlN barriers," p. 3.

[3] M. H. Wong, Y. Pei, J. S. Speck, and U. K. Mishra, "High power N-face GaN high electron mobility transistors grown by molecular beam epitaxy with optimization of AlN nucleation," *Appl. Phys. Lett.*, vol. 94, no. 18, p. 182103, May 2009.

[4] Man Hoi Wong, Yi Pei, D. F. Brown, S. Keller, J. S. Speck, and U. K. Mishra, "High-Performance N-Face GaN Microwave MIS-HEMTs With > 70% Power-Added Efficiency," *IEEE Electron Device Lett.*, vol. 30, no. 8, pp. 802–804, Aug. 2009.

[5] M. H. Wong *et al.*, "N-face high electron mobility transistors with a GaN-spacer," *Phys. Status Solidi A*, vol. 204, no. 6, pp. 2049–2053, Jun. 2007.

[6] E. Ahmadi, "Growth Optimization of III-N Electronic Devices by Plasma-Assisted Molecular Beam Epitaxy," p. 146.

[7] J. B. Khurgin, S. Bajaj, and S. Rajan, "Elastic scattering by hot electrons and apparent lifetime of longitudinal optical phonons in gallium nitride," *Appl. Phys. Lett.*, vol. 107, no. 26, p. 262101, Dec. 2015.

[8] S. Kolluri *et al.*, "Influence of AlN interlayer on the anisotropic electron mobility and the device characteristics of N-polar AlGaN/GaN metal-insulator-semiconductor-high electron mobility transistors grown on vicinal substrates," *J. Appl. Phys.*, vol. 108, no. 7, p. 074502, Oct. 2010.
[9] Bandeng 1D Poisson Schrodinger Solver

Appendices

A.1 Al-composition studies comparing Ga-polar and N-polar GaN grown by MBE:

In this section we show a history of Al-composition studies carried out over the course of a year on both Ga-polar and N-polar GaN at different growth temperatures. Unless otherwise stated, for all growths carried out in these appendices, growth conditions mirrored those described in section 4.2. Five Al-comp. studies are displayed in Fig. A.1.1. From the figure below, we see an exponential increase in Al-incorporation for a given cell temperature and a linear increase in Al-incorporation for a given Al BEP which is what would be expected considering temperature and partial pressure of source material in an effusion cell are exponentially related. The plots of the blue circles shown in the figure below (N-face (730 deg.) 2018) corresponds to the samples in the C-series study which was presented in section 4.6. For each of these studies 30-50 nm of AlGaN was deposited directly on bulk GaN (for the case of the 2018 sample) or on MOCVD grown GaN-on-sapphire templates (all other samples). From this data it can be concluded that Ga-polar films tend to incorporate more Al for a given Al-cell BEP (beam equivalent pressure) when compared to N-polar AlGaN. It is also observed that for Ga-polar films, going to higher growth temperatures results in higher Al-incorporation. The lower Al-incorporation seen in the N-polar films grown at 730^{o} (blue circles) when compared to the other N-polar films grown at 720^{o} (orange triangles and yellow stars) is likely related to growth rate; the N-polar films grown at 730^{o} (blue circles) were grown with a ~6 nm/min growth rate whereas all the other films grown in these studies were grown with a ~4.2 nm/min growth rate. Al-composition was determined by on-axis (0002) XRD $\omega - 2\theta$ scans.

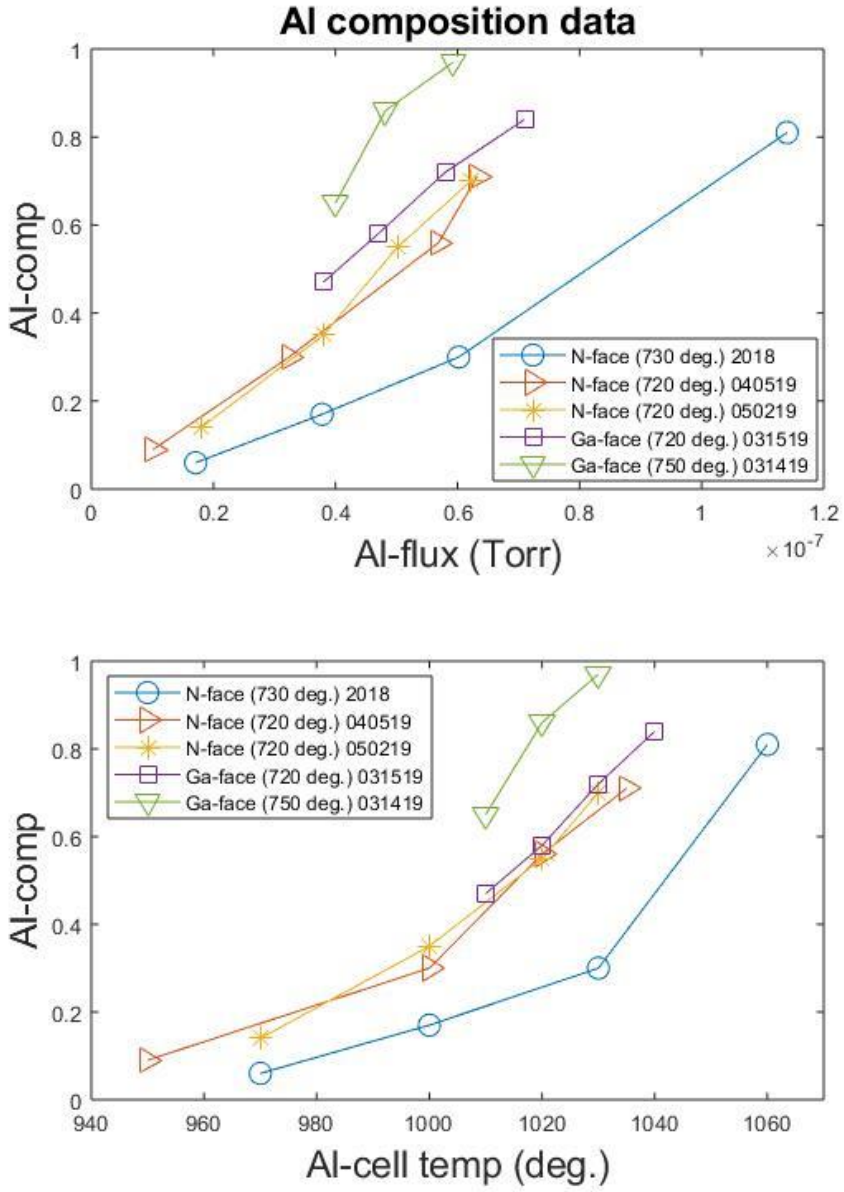

Figure A.1.1: Al-composition as a function of Al cell temperature and Al flux for a series of Al-composition studies carried out on Ga-polar and N-polar GaN and at different growth temperatures between 2018-2019.

A.2 N-polar growth rate calibration study at 720^{o}:

Growth rate calibration (GRC) studies can help to better comprehend how Ga-flux effects surface morphology and film quality. In this section a simple N-polar GRC study is presented which consisted of four samples, each initiated with 35 second of AlN followed by 15 minutes of GaN grown on a miscut GaN-on-sapphire template. Ga flux was varied 4.96e-7 torr to 1.57e-6 torr across four growths with a substrate temperature of 720^{o}. The details of each growth are given in table A.2.1 below, whereas, the corresponding AFM micrographs and XRD plots are show in Fig. A.2.1 below.

Table A.2.1: data for N-polar GRC series 032219

	MBE in-situ data			**XRD data**			**AFM data**	
sample	T(Ga) (deg. C)	F(Ga) (Torr)	final desorb (mm:ss)	FWHM (deg.)	thickness (nm)	GR (nm/min)	surf. desc.	(RMS) (nm)
0322A	1030	4.96e-7	-	0.082	36	2.4	3D	2.564
0322B	1070	8.96e-7	0.05	0.1	71	4.73	good	2.026
0322C	1095	1.26e-6	3:30	0.117	60	4	good	1.757
0322D	1110	1.57e-6	2:09	0.112	65	4.33	droplets	1.682

From table A.2.1 and Fig. A.2.1 we see an improvement in surface morphology as we go to higher Ga-fluxes. From this data it is clear that the growth rate saturates and then drops slightly for sample 0322B, therefor it can be concluded that a Ga-BEP of 8.96e-7 torr was sufficient to provide enough Ga-flux to maintain a Ga-adlayer during growth. AFM micrographs below illustrate how Ga-rich growth leads to smoother surface morphology. For the sample with the lowest Ga-flux (0322A) the surface is rough and grainy indicative of 3D growth. When the Ga-flux increases we see an improvement in surface morphology.

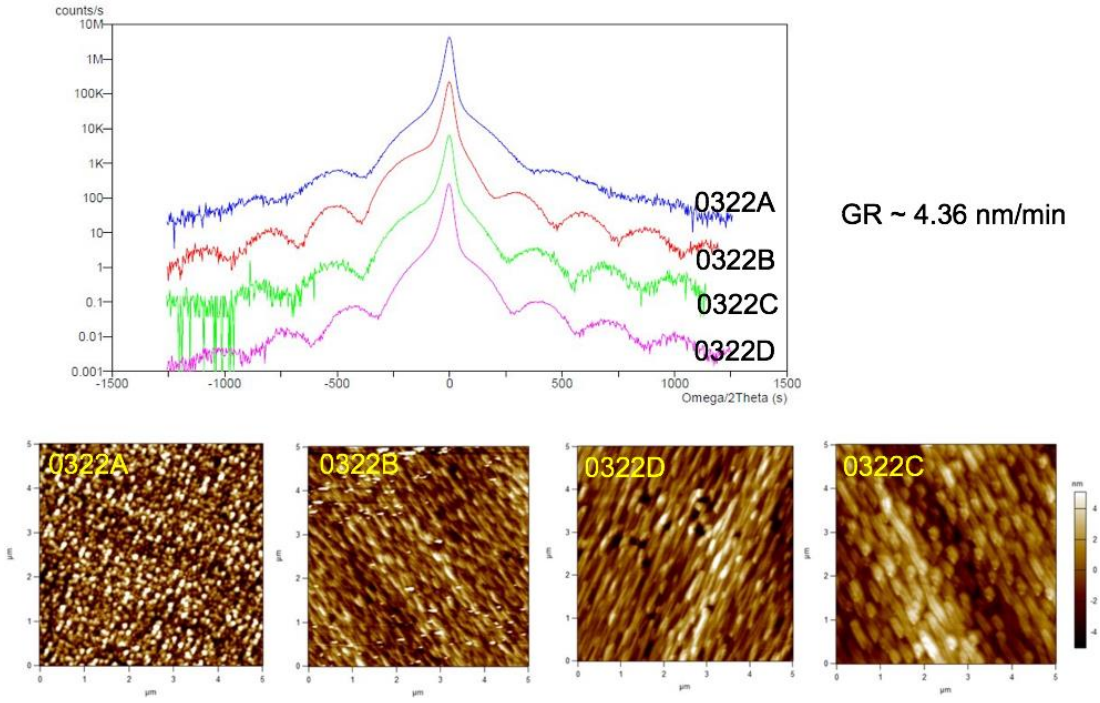

Fig. A.2.1: (Top) on-axis (0002) XRD $\omega - 2\theta$ scans for each sample (0322A-C). (below) AFM micrographs for the corresponding samples.

A.3 Checking for polarity via a KOH-dip:

In section 4.5 it was shown how polarity inversion was ruled out by using CBED. CBED is an extremely accurate method for checking the crystal orientation of GaN, however, it involves costly and time-consuming TEM work. Given the sensitively of the N-face surface, many chemicals tend to roughen and etch N-polar GaN. Chemicals such as potassium hydroxide (KOH), hydrochloric acid (HCl) as well as many alkali-based photoresist developers tend to etch and roughen the N-polar surface. In this study two samples were prepared, one of which was a Ga-polar GaN-on-sapphire template and another sample which consisted of 100 nm of MBE-grown GaN on bulk GaN using the 2 nm AIL described in section 4.4. AFM micrographs were taken before and after a 5 min dip in KOH. The resulting AFM micrographs are displayed in Fig. A.3.1 below.

From Fig. A.3.1 we see a clear sign of roughening of the N-polar surface while the Ga-polar surface looks almost completely unchanged. Thus a simple, yet destructive, method is demonstrated for verifying the polarity of GaN.

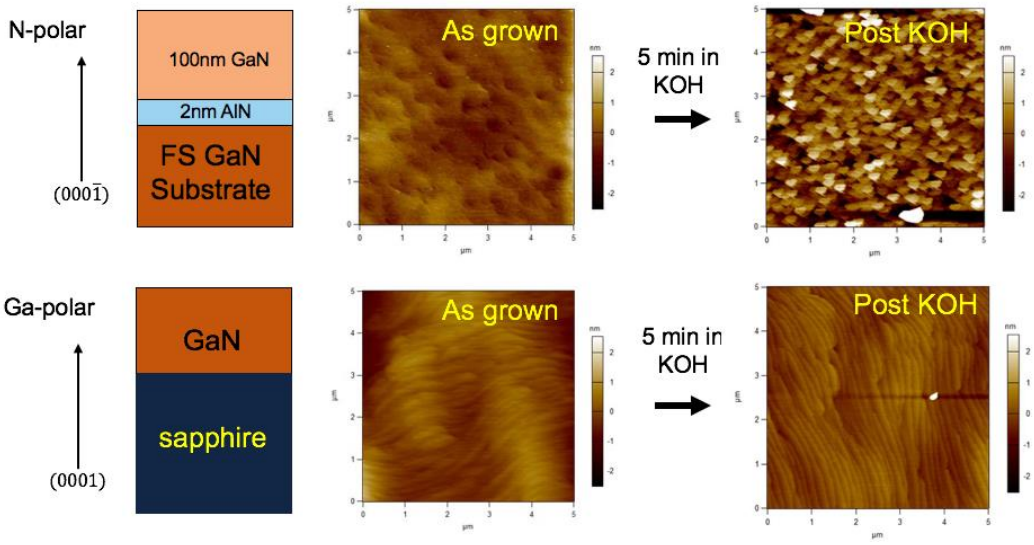

Fig. A.3.1: demonstration of testing polarity of GaN by KOH dip. (Top) N-polar film before and after a 5 min KOH dip. (Below) Ga-polar films before and after a 5 min KOH dip.

A.4 Verifying UID carrier concentration in N-polar GaN grown on bulk GaN by PAMBE:

In this study one sample was grown on a semi-insulating bulk GaN substrate using the 2 nm AIL followed by 500 nm of UID GaN. Surface morphology was verified by AFM followed by room temperature (RT) Van der Pauw Hall measurement to obtain the UID carrier concentration. Using Bandeng, both the band diagram and charge profile were simulated for this structure with the carrier concentration obtained from Hall. A UID donor concentration of 5.16e17 cm^{-3} was found from Hall which is more than two orders of magnitude higher than the O-concentration and Si-concentration seen in the SIMS results in Fig. 4.2.2. Therefor it can be concluded that either there is a large concentration of N-vacancies in the film or there is another donor present responsible for the high charge. Fig. A.4.1 below shows the AFM micrograph and simulated band and charge profile for the sample in this study.

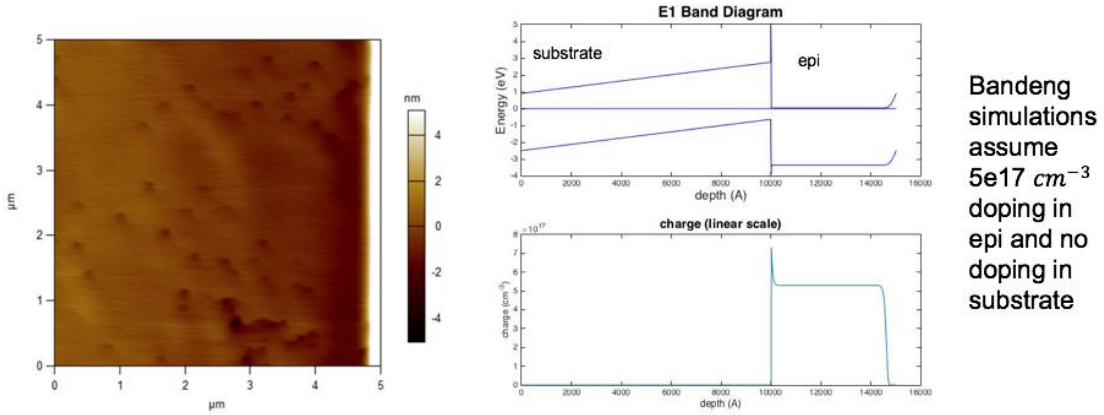

Fig. A.4.1: (left) AFM micrograph for 500 nm N-polar GaN grown by PAMBE on bulk GaN using a 2 nm AIL. (right) simulated band diagram and charge profile of said structure with the UID carrier concentration 5e17 cm^{-3} obtained from RT-Hall.

A.5 Carbon doping SIMS results:

To obtain C-concentration as a function of CBr_4 foreline pressure (explained in section 4.2), SIMS was carried out on a sample with four C-doped layers of different CBr_4 foreline pressure. The structure and resulting SIMS results are displayed in Fig. A.5.1 below. As can be observed in Fig. A.5.1 C-doping is not very abrupt in between the AlGaN spacer layers. This is possibly caused by two reasons. Firstly, it is believed that the C-doping diffuse through the film during growth even after the valve from the CBr_4 line is closed. Secondly, since the CBr_4 pressure is controlled by a foreline which travels from a valve outside of the chamber rather than an effusion cell shutter, there is most likely a delay is CBr_4 pressure as the valve is opened and closed.

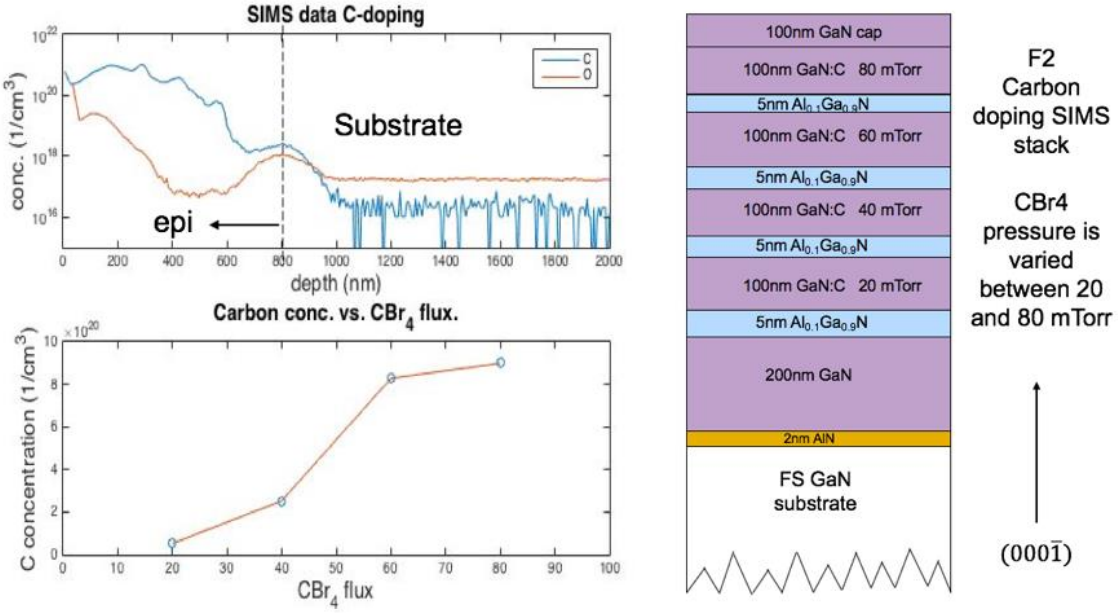

Fig. A.5.1: SIMS results for C-doping via CBr_4 foreline pressure. (right) structure, (left) SIMS plot